

1

2 Rotavirus spike protein VP<sub>4</sub> mediates viroplasm assembly by association to  
3 actin filaments.

4

5 Janine Vetter<sup>a,1</sup>, Guido Papa<sup>b,1,\*</sup>, Michael Seyffert<sup>a</sup>, Kapila Gunasekera<sup>c</sup>, Giuditta De

6 Lorenzo<sup>b,\*</sup>, Mahesa Wiesendanger<sup>a,d</sup>, Jean-Louis Reymond<sup>c</sup>, Cornel Fraefel<sup>a</sup>, Oscar R.

7 Burrone<sup>b</sup>, Catherine Eichwald<sup>a,#</sup>.

8 <sup>a</sup>Institute of Virology, University of Zurich, Zurich, Switzerland.

9 <sup>b</sup>Molecular Immunology Laboratory, International Centre for Genetic Engineering and  
10 Biotechnology, Trieste, Italy.

11 <sup>c</sup>Department of Chemistry and Biochemistry and Pharmaceutical Sciences, University of  
12 Bern, Bern, Switzerland.

13 <sup>d</sup>Institute of Anatomy, Vetsuisse, University of Zurich, Zurich, Switzerland

14

15 Running Head: New role of rotavirus VP<sub>4</sub>

16

17 **#Address correspondence to** Catherine Eichwald, [ceichwald@vetvir.uzh.ch](mailto:ceichwald@vetvir.uzh.ch)

18 **<sup>1</sup>Author Contributions:** GP and JV contributed equally to this work.

19 **\*Present address:** GP: MRC Laboratory of Molecular Biology, Cambridge, UK; and GDL:

20 MRC-University of Glasgow, Centre for Virus Research, Glasgow, UK

21 **Keywords:** rotavirus, spike-protein, viroplasm, VP<sub>4</sub>, reverse-genetics.

22

23

24 **Abstract**

25 The formation of viroplasm is a well-conserved step in the rotavirus (RV) life cycle. In these  
26 structures, both virus genome replication and progeny assembly take place. A stabilized  
27 microtubule cytoskeleton and lipid droplets are required for the viroplasm formation, which  
28 involves several virus proteins. The viral spike protein VP<sub>4</sub> has not previously been shown to  
29 have a direct role in viroplasm formation. However, it is involved with virus-cell attachment,  
30 endocytic internalization, and virion morphogenesis. Moreover, VP<sub>4</sub> interacts with actin  
31 cytoskeleton components, mainly in processes involving virus entrance and egress, and  
32 thereby may have an indirect role in viroplasm formation. In this study, we used reverse  
33 genetics to construct a recombinant RV, rRV/VP<sub>4</sub>-BAP, which contains a biotin acceptor  
34 peptide (BAP) in the K<sub>145</sub>-G<sub>150</sub> loop of the VP<sub>4</sub> lectin domain, permitting live monitoring.  
35 The recombinant virus was replication competent but showed a reduced fitness. We  
36 demonstrate that rRV/VP<sub>4</sub>-BAP infection, as opposed to rRV/wt infection, did not lead to a  
37 reorganized actin cytoskeleton as viroplasms formed were insensitive to drugs that  
38 depolymerize actin and inhibit myosin. Moreover, wt VP<sub>4</sub>, but not VP<sub>4</sub>-BAP, appeared to  
39 associate with actin filaments. Similarly, VP<sub>4</sub> in co-expression with NSP<sub>5</sub> and NSP<sub>2</sub> induced  
40 a significant increase in the number of viroplasm-like structures. Interestingly, a small  
41 peptide mimicking loop K<sub>145</sub>-G<sub>150</sub> rescued the phenotype of rRV/VP<sub>4</sub>-BAP by increasing  
42 its ability to form viroplasms and hence, improve virus progeny formation. Collectively,  
43 these results provide a direct link between VP<sub>4</sub> and the actin cytoskeleton to catalyze  
44 viroplasm assembly.

45

46 **IMPORTANCE** The spike protein VP<sub>4</sub> participates in diverse steps of the rotavirus (RV) life  
47 cycle, including virus-cell attachment, internalization, modulation of endocytosis, virion  
48 morphogenesis, and virus egress. Using reverse genetics, we constructed for the first time a  
49 recombinant RV, rRV/VP<sub>4</sub>-BAP, harboring a heterologous peptide in the lectin domain  
50 (loop K<sub>145</sub>-G<sub>150</sub>) of VP<sub>4</sub>. The rRV/VP<sub>4</sub>-BAP was replication-competent but with reduced  
51 fitness due to a defect in the ability to reorganize the actin cytoskeleton, which affected the  
52 efficiency of viroplasm assembly. This defect was rescued by adding a permeable small-  
53 peptide mimicking the wild-type VP<sub>4</sub> loop K<sub>145</sub>-G<sub>150</sub>. In addition to revealing a new role of  
54 VP<sub>4</sub>, our findings suggest that rRV harboring an engineered VP<sub>4</sub> could be used as a new  
55 dual vaccination platform providing immunity against RV and additional heterologous  
56 antigens.

57

## 58 Introduction

59 Rotavirus (RV) is the primary etiological agent responsible for severe gastroenteritis  
60 and dehydration in infants and young children worldwide (1), resulting in the death of  
61 128'000 children under five years of age in developing countries. Moreover, it also infects  
62 young animals such as piglets, calves, and poultry, negatively impacting the livestock  
63 industry (2-4).

64 RV virions are non-enveloped icosahedral particles composed of three concentric  
65 layers, called triple-layered particles (TLPs). The virus core-shell encloses eleven double-  
66 stranded (ds) RNA genome segments and twelve copies of both the RNA-dependent RNA  
67 polymerase, VP1, and the guanyl-methyltransferase, VP3 (5, 6). The icosahedral core-shell  
68 (T=1, symmetry) is composed of twelve decamers of VP2 and surrounded by 260 trimers of  
69 the structural protein VP6, constituting transcriptionally active double-layered particles  
70 (DLPs) (7, 8). Trimers of VP7 glycoprotein organized in an icosahedral symmetry (T=13)  
71 stand on the top of each VP6 trimer constituting the main building component of the virion  
72 outer layer. The spike protein VP4 anchors at each of the virion 5-fold axes adopting a  
73 trimeric conformation although having a dimeric appearance when visualized from the top  
74 of the capsid surface (9-12).

75 Immediately after RV internalization, the DLPs are released into the cytoplasm and  
76 become transcriptionally active (13), leading to the first round of transcription, which is  
77 necessary for halting the host innate immune response (14-18), shutting off the host  
78 translation machinery (19), and starting the building-up of viroplasms (20-22). The RV  
79 cytosolic replication compartments, termed viroplasms, are membrane-less electron-dense  
80 globular inclusions responsible for virus genome replication and virus progeny assembly  
81 (20, 23). The RV proteins NSP5, NSP2, and VP2 are the assembling blocks for viroplasms

82 (24). Other virus proteins are also found in the viroplasms, including NSP<sub>4</sub>, VP<sub>1</sub>, VP<sub>3</sub>, and  
83 VP<sub>6</sub>, together with double-stranded and single-stranded viral RNAs. Host components,  
84 such as microtubules, lipid droplets, or miRNA-7 (25-27) are also recruited to viroplasms.  
85 The formation of viroplasms requires the reorganization and stabilization of the  
86 microtubule network and the recruitment of lipid droplets in a process directly associated  
87 with NSP<sub>2</sub> and VP<sub>2</sub>. Thus, to be formed, the viroplasms have to coalesce from small-  
88 punctuated structures diffused in the cytosol at early times of infection to perinuclear large-  
89 mature viroplasms at late times of infection (25, 26, 28). However, pieces of evidence  
90 suggest that not only microtubules but also actin and intermediate filaments reorganize  
91 under RV infection by using a mechanism not yet described (25, 29). Many virus proteins  
92 have multifunctional roles during the viral life cycle, and the RV proteins are no exception.  
93 An example is VP<sub>4</sub> which is cleaved by a trypsin-like enzyme found in the intestinal tract  
94 (30) into two main products, VP8\* (28 kDa, amino acids 1-247) and VP5\* (60 kDa, amino  
95 acids 248-776) that remain non-covalently associated with the infectious RV virion allowing  
96 the initialization of the virus entry process (31, 32). VP8\* and a significant portion of VP5\*,  
97 VP5CT (amino acids 246-477), constitute the distal globular and the central body of the  
98 spike, respectively (33, 34). The VP8\* subunit has several functions, such as haemagglutinin  
99 activity (35), involvement in binding the host sialic acid (34), and a determinant role in virus  
100 tropism. VP5\* has been implicated in the interaction with integrins (36-38). During virus  
101 internalization, VP<sub>4</sub> engages the endocytic pathway (39, 40) by binding to the small  
102 GTPase Rab5 and PRA1 within early endosomes (41), directly activating hsp70 (42, 43) and  
103 associating with the actin-binding protein Drebrin 1, an RV restriction factor (44). VP<sub>4</sub> also  
104 plays an essential role in virion morphogenesis and can be found as a soluble protein in the  
105 cytosol (45). When expressed in the absence of other RV proteins, VP<sub>4</sub> is associated with

106 the microtubules and the actin cytoskeleton (45-50). In polarized cells, VP<sub>4</sub> seems to  
107 interact with the apical actin cortex, leading to the remodeling of the brush border and  
108 subsequently releasing the RV virions into the medium (48). This actin association is  
109 dependent on a VP<sub>4</sub> actin-binding domain present at its C-terminus (residues 713-776) in  
110 cooperation with the coiled-coil domain (residues 481-574) (45). However, there is no direct  
111 evidence that VP<sub>4</sub> participates in actin reorganization during RV infection.

112 Here, we describe the generation of a recombinant RV (rRV) harboring a genetically  
113 modified genome segment 4 (gs<sub>4</sub>) encoding the spike protein VP<sub>4</sub> with a biotin-aceptor  
114 peptide (BAP) tag of 15 amino acids inserted in an exposed loop of VP8\* (residues K145-  
115 G150). Even though rRV/VP<sub>4</sub>-BAP is internalized and able to produce virus progeny, it has  
116 significantly reduced virus fitness because of an impaired ability of VP<sub>4</sub>-BAP to associate  
117 with the actin cytoskeleton. In addition, we provide clear evidence that VP<sub>4</sub> acts as a  
118 catalyst for the assembly of the viroplasm in an actin-dependent process.

119

## 120 **Results**

121 **Production and analysis of recombinant rotavirus harboring a BAP tagged spike**  
122 **protein.** As the VP<sub>4</sub> spike protein plays an essential role in the host cell tropism,  
123 attachment, and internalization, we addressed if VP<sub>4</sub> could be engineered by incorporating  
124 a heterologous peptidic tag within its coding sequence without compromising its structural  
125 and functional properties. To test this hypothesis, we identified in the previously published  
126 crystal structure of simian RRV VP<sub>4</sub> (10) four different exposed loops localized in the lectin  
127 domain (amino acids 65-224) of the VP8\* subunit and then inserted a biotin aceptor  
128 peptide (BAP) tag (51, 52) in each of the corresponding loops of the VP<sub>4</sub> simian strain SA11.  
129 As depicted in **Fig. 1a**, the selected loops for the BAP tag insertions were T96-R101, E109-

130 S<sub>114</sub>, N<sub>132</sub>-Q<sub>137</sub>, and K<sub>145</sub>-G<sub>150</sub>, labeled with the colors blue, orange, pink, and green,  
131 respectively. First, we assessed the biotinylation of these four BAP-tagged VP<sub>4</sub> proteins,  
132 herein VP<sub>4</sub>-BAP, in cell lysates by western blot-retardation assay (WB-ra) (51). For this  
133 purpose, each construct was co-expressed with cytosolically localized biotin ligase Bir A  
134 (cyt-BirA) in MA<sub>104</sub> cells infected with recombinant vaccinia virus encoding T<sub>7</sub> RNA  
135 polymerase to allow the synthesis of cytosolic VP<sub>4</sub> transcripts. As the synthesis of nuclear  
136 VP<sub>4</sub> transcripts promotes undesired mRNA splicing (53), we used a T<sub>7</sub> promoter to favor  
137 cytosolic transcription provided by the T<sub>7</sub> RNA polymerase. As shown in **Fig. 1b**, the four  
138 VP<sub>4</sub>-BAP variants (**Fig. 1b, lanes 4, 6, 8 and 10**), but not the wild type (wt) VP<sub>4</sub> (**Fig. 1b,**  
139 **lane 2**), were fully biotinylated when the cell extracts were incubated with streptavidin  
140 (StAv), generating a band shift of approximately 140 kDa that corresponds to the VP<sub>4</sub>-  
141 BAP/StAv complex. Of note, biotinylated protein-StAV complexes hinder epitopes of the  
142 biotinylated protein denoted as a shifted and weaker band in western blot. The band  
143 observed immediately above the VP<sub>4</sub>-BAP band (80 kDa) represents a phosphorylated  
144 form of the protein that is only present in transfected cells but not in RV-infected cells, as  
145 demonstrated by the λ-phosphatase treatment of the cellular extracts (**Fig. S1a and b**).  
146 This result suggests that the expression and stability of the different VP<sub>4</sub>-BAP proteins  
147 were not affected by the location of the inserted BAP tag.

148         Next, we assessed whether the four VP<sub>4</sub>-BAP proteins could assemble into  
149 infectious RV particles and support virus replication. To rescue recombinant rotavirus (rRV)  
150 harboring a genetically modified genome segment 4 (gs<sub>4</sub>) encoding for the different VP<sub>4</sub>-  
151 BAP proteins (gs<sub>4</sub>-BAP), we took advantage of the previously established reverse genetics  
152 system (54). Of the four different constructs, we successfully rescued only the rRV  
153 harboring gs<sub>4</sub>-BAP encoding the BAP tag within the K<sub>145</sub>-G<sub>150</sub> loop in VP8\* (**Fig. 1a**),

154 herein named rRV/VP<sub>4</sub>-BAP. The rescued virus was confirmed by the differential migration  
155 pattern of the modified gs<sub>4</sub>-BAP compared to the wt gs<sub>4</sub> (**Fig. 1c**) and by Sanger  
156 sequencing (**Fig. 1d**). Notably, the genome segment 4 (gs<sub>4</sub>-BAP) and all the other ten  
157 genome segments of rRV/VP<sub>4</sub> were stable in tissue culture at least until virus passage ten  
158 as determined by Sanger sequencing and deep sequencing (**Fig S1b and supplementary**  
159 **information**). We then investigated the ability of rRV/VP<sub>4</sub>-BAP to express biotinylated  
160 VP<sub>4</sub>-BAP. Specifically, cell extracts of rRV/VP<sub>4</sub>-BAP infected MA/cytBirA cells (MA<sub>104</sub> cells  
161 stably expressing cytosolic localized BirA) were analyzed at 6 hpi by western blot. Thus, the  
162 produced VP<sub>4</sub>-BAP protein showed to be biotinylated as demonstrated after incubation  
163 with StAv-peroxidase, which detected a band of approx. 85 kDa only in rRV/VP<sub>4</sub>-BAP  
164 infected MA/cytBirA cell extracts but not in rRV/VP<sub>4</sub>-BAP-infected MA<sub>104</sub> cells (**Fig. 1e,**  
165 **lane 3 and 6**). As expected, VP<sub>4</sub> biotinylation was detected neither in rRV/wt infected  
166 MA/cytBirA cells nor in rRV/VP<sub>4</sub>-BAP infected MA<sub>104</sub> cells (**Fig. 1e, lanes 2, 5, and 6**). We  
167 found by WB-ra that the fraction of biotinylated VP<sub>4</sub>-BAP corresponds to 48 % of the total  
168 protein (**Fig. 1f**).

169 We next examined if the biotinylated virus-encoded VP<sub>4</sub>-BAP is incorporated into  
170 newly assembled virus particles. For this, we purified rRV/VP<sub>4</sub>-BAP virions produced in  
171 MA/cytBirA cells in the absence or presence of biotin and visualized the virus particles by  
172 negative staining electron microscopy after incubation with StAv conjugated to gold  
173 particles. Thus, 53% of the virions produced in the presence of biotin were decorated with  
174 StAV-gold particles (**Fig. 1g**) but none in the unbiotinylated control particles. Similarly,  
175 indirect ELISA with identical amounts of unbiotinylated and biotinylated purified rRV/VP<sub>4</sub>-  
176 BAP revealed a signal upon StAV-peroxidase staining only for biotinylated samples.  
177 Furthermore, similar signals were observed in ELISA using an anti-rotavirus antibody (**Fig.**



178 **1h**). These outcomes collectively suggest that virus-encoded VP<sub>4</sub>-BAP is biotinylated and  
179 incorporated in newly formed RV particles. Interestingly, as shown in **Fig. 1i**, the rRV/VP<sub>4</sub>  
180 particles appear to have a slightly larger diameter (~80 nm) when compared to rRV/wt  
181 particles (~75 nm) but were still in the range of TLPs (55).

182 **Subcellular localization of rRV/VP<sub>4</sub>-BAP.** We investigated the subcellular localization of  
183 the newly produced biotinylated VP<sub>4</sub>-BAP in rRV/VP<sub>4</sub>-BAP infected cells at 6 hpi, a time  
184 point showing well-assembled viroplasms (25). For this, both rRV/wt and rRV/VP<sub>4</sub>-BAP-  
185 infected MA/cytBirA cells were incubated in the absence or presence of biotin for 4 hours  
186 before fixation. Biotinylated VP<sub>4</sub>-BAP detected with StAv-Alexa 555 was found  
187 surrounding the viroplasms (stained anti-NSP5) (**Fig. 2a**). However, no StAv-Alexa 555  
188 signal was detected in cells infected with either rRV/wt or rRV/VP<sub>4</sub>-BAP without biotin.  
189 Notably, the biotinylated VP<sub>4</sub>-BAP partially co-localized with trimeric VP7 in the  
190 endoplasmic reticulum (ER) (**Fig. 2b**). Additionally, the cytosolic distribution of VP<sub>4</sub>-BAP  
191 was similar to that of VP<sub>4</sub> in rRV/wt-infect cells (**Fig. 2c**). These results suggest that the  
192 modification exerted in VP<sub>4</sub>-BAP does not impact VP<sub>4</sub> subcellular localization in infected  
193 cells.

194 **Impaired virus fitness of rRV/VP<sub>4</sub>-BAP.** To compare the replication fitness of rRV/VP<sub>4</sub>-  
195 BAP with that of rRV/wt, we infected MA104 cells at equal MOI and harvested the virus at  
196 various time points until 48 hpi. As depicted in **Fig 3a**, rRV/VP<sub>4</sub>-BAP showed a significantly  
197 delayed fitness curve compared to rRV/wt. To investigate this divergence in the virus  
198 replication, we infected cells with identical MOI (**Fig. 3b**) or an equal number of virus  
199 particles (**Fig. 3c**) and quantified cells showing viroplasms at 6 hpi. In both experimental  
200 conditions, we observed a significantly reduced ratio of cells containing viroplasms upon  
201 rRV/VP<sub>4</sub>-BAP infection when compared with rRV/wt infection.

202 **Comparable entry processes between rRV/wt and rRV/VP<sub>4</sub>-BAP.** Since VP<sub>4</sub> has an  
203 essential role in virus-cell attachment, we interrogated whether the ability of rRV/VP<sub>4</sub>-BAP  
204 particles to bind to cells was impaired. To test this hypothesis, we performed a  
205 nonradioactive binding assay described previously by Zarate *et al.* (56) to compare the  
206 attachment to MA<sub>104</sub> cells with different amounts of either rRV/wt or rRV/VP<sub>4</sub>-BAP. As  
207 depicted in **Fig 4a**, no differences in cell attachment were observed among the two viruses.  
208 Of note, the antibody conditions used for the virus detection are in the linear range (**Fig**  
209 **S2a**). Moreover, biotin-labeled rRV/VP<sub>4</sub> did not hinder the virus-cell attachment as denoted  
210 by the same results for the attachment of both unbiotinylated and biotinylated rRV/VP<sub>4</sub>-  
211 BAP virus particles (**Fig 4b**). As expected, binding of rRV/VP<sub>4</sub>-BAP was detected with  
212 StAVonly when grown in the presence of biotin (**Fig 4c**).

213         Next, we investigated whether the delay in viral replication fitness was caused by a  
214 difference in virus internalization. Purified rRV/VP<sub>4</sub>-BAP and rRV/wt virions were compared  
215 and analyzed for virus internalization by confocal scanning laser microscopy (CSLM) using  
216 immunostaining with the conformational monoclonal antibody anti-VP7 (clone 159), which  
217 only recognizes the trimeric form of the VP7 protein (57, 58). As a control, purified rRV/VP<sub>4</sub>-  
218 BAP, but not rRV/wt, was directly labeled with StrAv-Alexa 555 prior to infection. Initially (0  
219 min), VP<sub>4</sub>-BAP and VP7 signals co-localized on the cell surface, indicating the association of  
220 virions to the cell membrane. However, after two minutes at 37°C, both signals were  
221 already internalized (**Fig 4d**). The localization patterns were comparable to those observed  
222 at the same time points with rRV/wt virions, suggesting no differences in the internalization  
223 mechanism between the two viruses.

224         Since virus-cell attachment and virus internalization were comparable between  
225 rRV/wt and rRV/VP<sub>4</sub>, we investigated if virus transcription was defective or delayed for

226 rRV/VP<sub>4</sub>-BAP. Thus, we compared the abundance of NSP<sub>5</sub> and VP<sub>6</sub> virus transcripts at 4  
227 hpi of MA<sub>104</sub> cells infected with either rRV/wt or rRV/VP<sub>4</sub>-BAP. As denoted in **Figs 4e-g**,  
228 the transcription levels of NSP<sub>5</sub>, VP<sub>6</sub>, and the housekeeping gene SDHA were comparable  
229 in cells infected with rRV/wt or rRV/VP<sub>4</sub>-BAP.

230 **rRV/VP<sub>4</sub>-BAP has a defect in a step between virus transcription and viroplasm**  
231 **formation.** We analyzed by high-definition electron microscopy the structural morphology  
232 of the viroplasms from rRV/wt or rRV/VP<sub>4</sub>-BAP at two time points, 6 and 12 hpi, which for  
233 simian strain SA<sub>11</sub> corresponds to a time showing well-formed viroplasms and a time with  
234 highly mature viroplasms, respectively (**Fig 5a**). No apparent differences in the viroplasm  
235 morphology were observed between the two viruses at 6 and 12 hpi. Similarly, we  
236 examined whether the liquid-liquid phase separation properties of rRV/VP<sub>4</sub>-BAP  
237 viroplasms were modified. For this, we took advantage of our previously established  
238 MA<sub>104</sub> cell line stably expressing NSP<sub>2</sub>-mCherry (MA/NSP<sub>2</sub>-mCherry) to visualize  
239 viroplasm formation in living cells because of the ability of this protein to get recruited into  
240 viroplasms during RV infection (21, 25, 59). Next, we measured the NSP<sub>2</sub>-mCherry diffusion  
241 dynamics in single viroplasms using fluorescence recovery after photobleaching (FRAP)  
242 experiments (**Fig 5b and c**). We found that FRAP properties concerning NSP<sub>2</sub>-mCherry  
243 half-time recovery and mobility were similar for both viruses (**Fig. 5d and e**).

244 To confirm our results and exclude the involvement of the endocytic pathway, we  
245 purified and transfected MA<sub>104</sub> cells with an equal number of DLPs of the two viruses (**Fig**  
246 **6a**). Of note, purified rRV/wt DLPs or rRV/VP<sub>4</sub>-BAP DLPs had the same size, while  
247 rRV/VP<sub>4</sub>-BAP TLPs were larger than rRV/wt TLPs (**Fig 1i and 6a**). At 6 h after transfection,  
248 we observed identical expression of NSP<sub>5</sub> for both viruses, as denoted by in-cell western  
249 assay (**Figs 6b and c**). In the same experimental setting, the number of cells showing

250 viroplasms (detected with anti-NSP5) was significantly reduced in rRV/VP<sub>4</sub>-BAP infected  
251 cells compared to rRV/wt infected cells (**Figs 6d and e**). These outcomes strongly suggest  
252 that the reduced replication fitness of rRV/VP<sub>4</sub>-BAP involves a step in viroplasm assembly.  
253 **VP<sub>4</sub> promotes viroplasm assembly.** Since we hypothesized that VP<sub>4</sub> may have a yet  
254 unidentified role in the viroplasm assembly, we investigated if spontaneous disruption of  
255 the viroplasm led to a delayed re-assembly of these structures. To challenge this  
256 hypothesis, we used 1,6-hexanediol (1,6-HD), a well-described aliphatic alcohol able to  
257 disrupt key drivers of liquid-liquid phase separation and recently shown to be effective in  
258 dissolving RV viroplasms (28) and determined the recovery of NSP2-mCherry in viroplasms.  
259 For this, MA/NSP2-mCherry cells at 5 h after infection with either rRV/VP<sub>4</sub>-BAP or rRV/wt  
260 were treated for 6 min with 1,6-HD and observed for 30 min after washout of the  
261 compound (**Fig. 7a and b**). Interestingly, the recovery kinetic of rRV/VP<sub>4</sub>-BAP viroplasms  
262 was delayed compared to that of rRV/wt at short times after removing the drug (2 min), as  
263 confirmed by both a reduced ratio of cells presenting viroplasms (**Fig. 7c**) and a reduced  
264 number of viroplasm per cell (**Fig. 7d**). In order to further characterize the relationship  
265 between viroplasms and VP<sub>4</sub>, we performed transcriptional silencing experiments with VP<sub>4</sub>  
266 specific siRNAs (siVP<sub>4</sub>) in MA/NSP2-mCherry cells (**Fig. 7e**). In this context, it has been  
267 previously described that the silencing of VP<sub>4</sub> during RV infection leads to viroplasm  
268 formation even if TLPs assembly is impaired (60). We then monitored viroplasm formation  
269 in siVP<sub>4</sub> and control-siRNA (scr) transfected MA104 cells infected with simian strain SA11  
270 and treated with 1,6-HD as described for the experiment shown in **Fig 7a**. The viroplasms  
271 produced on VP<sub>4</sub> silenced cells had a delayed recovery kinetic similarly to that observed for  
272 rRV/VP<sub>4</sub>-BAP viroplasms (**Fig 7f and g**). Furthermore, similarly to **Fig 7d**, the number of  
273 viroplasms per cell was significantly decreased in siVP<sub>4</sub> treated cells at 2 min of recovery

274 compared to the experimental controls (**Fig 7h**). Thus, these results strongly suggest that  
275 VP<sub>4</sub> promotes either indirectly or directly the assembly of viroplasms.

276 **VP<sub>4</sub>-BAP impairs VLS assembly and association to actin filaments.** Viroplasm-like  
277 structures (VLS) are simplified models for the study of complex viroplasm structures,  
278 requiring the co-expression of NSP<sub>5</sub> with either NSP<sub>2</sub> (24) or VP<sub>2</sub> (22) to form globular  
279 cytosolic inclusions morphologically similar to viroplasms but unable to replicate and  
280 produce virus progeny. Considering this rationale, we formed VLSs by expressing NSP<sub>5</sub> and  
281 NSP<sub>2</sub> in the presence of GFP, VP<sub>4</sub>-GFP, or VP<sub>4</sub>-BAP-GFP (**Fig 8a**). We noticed the absence  
282 of co-localization of either VP<sub>4</sub>-GFP or VP<sub>4</sub>-BAP-GFP in VLSs. Furthermore, when we  
283 quantified the number of VLSs per cell (**Fig 8b**), we noticed that the number of VLSs  
284 formed in the presence of VP<sub>4</sub>-GFP was much larger than that produced in the presence of  
285 VP<sub>4</sub>-BAP-GFP or GFP.

286 Since VP<sub>4</sub> associates with actin cytoskeleton components (45, 47, 48), we  
287 hypothesized that VP<sub>4</sub>-BAP-GFP could have an impaired association with actin filaments.  
288 To investigate this possibility, MA<sub>104</sub> cells expressing VP<sub>4</sub>-GFP or VP<sub>4</sub>-BAP-GFP were  
289 untreated or treated with nocodazole for 1h before fixation. Nocodazole treatment induces  
290 depolymerization of the microtubule network permitting direct characterization of proteins  
291 associated with the actin cytoskeleton. In this context (**Fig 8c**), we stained the cells to  
292 detect actin cytoskeleton and noticed that VP<sub>4</sub>-GFP was associated, as expected, with  
293 actin filaments even after nocodazole treatment; while VP<sub>4</sub>-BAP-GFP was associated with  
294 filaments only in the absence of nocodazole. In MT-depolymerized cells, VP<sub>4</sub>-BAP-GFP  
295 formed diffuse small cytosolic aggregates or short filaments. Moreover, while the length of  
296 VP<sub>4</sub>-GFP fibers was comparable in the presence or absence of nocodazole treatment, the  
297 VP<sub>4</sub>-BAP-GFP fibers were significantly shorter in cells treated with nocodazole (**Fig 8d**),

298 suggesting an impaired association of VP<sub>4</sub>-BAP with actin filaments. Taken together, these  
299 results suggest that VP<sub>4</sub> promotes the assembly of VLSs mediated by its association with  
300 actin filaments.

301 **Impaired association between the actin cytoskeleton and rRV/VP<sub>4</sub>-BAP results in**  
302 **delayed viroplasm assembly.** RV strain SA11 infection (**Fig 9a** and (25, 61)) reorganizes the  
303 actin cytoskeleton, mainly by decreasing the actin stress fiber and redistributing it to the  
304 cell cortex. However, this reorganization did not take place in cells infected with rRV/VP<sub>4</sub>-  
305 BAP (**Fig 9b** and **Fig S3a**) featured by an increment in stress fibers surrounding the  
306 viroplasms (**Fig 9b**, yellow open arrows) and contrasting by an actin cell cortex increment in  
307 rRV/wt infected cells. Moreover, the actin cytoskeleton is not properly reorganized even in  
308 experiments with an increased rRV/VP<sub>4</sub>-BAP multiplicity of infection (**Fig. S3b**).  
309 Interestingly, the MT-network reorganization was attained by both viruses.

310 The cell has a contractile system regulated in part by the reorganization of stress  
311 fibers composed by actin and myosin II. We questioned if the molecular motor myosin was  
312 also required for viroplasm assembly and if its activity was impaired in rRV/VP<sub>4</sub>-BAP  
313 infected cells. For this purpose, we inspected the localization of paralog myosin IIa in cells  
314 infected with either rRV/wt or rRV/VP<sub>4</sub>-BAP at 6 hpi and compared it with non-infected  
315 conditions (**Fig 9c**). In non-infected cells, myosin IIa is homogeneously distributed in  
316 filaments, stacks, clusters, and continuous structures (62). However, upon rRV/wt infection,  
317 continuous myosin structures are lost, and myosin clusters and stacks in the cell cortex are  
318 favored (**Fig 9c**, yellow open arrowheads). In contrast, rRV/VP<sub>4</sub>-BAP infected cells still have  
319 continuous structures, mainly in the ventral cell region. Interestingly, VP<sub>4</sub> fibrillar  
320 morphology is observed in rRV/wt infected cells (**Fig 9b** and **c**, red open arrows) but not in  
321 rRV/VP<sub>4</sub>-BAP infected cells.

322 We confirmed the active role of the actin cytoskeleton in the assembly of rRV/wt  
323 and rRV/VP<sub>4</sub>-BAP viroplasms by adding actin inhibitors jasplakinolide (jasp) and  
324 cytochalasin B (cyt B) at 1 hpi, a time in which virus internalization and primary virus  
325 transcription are well-initiated (**Fig 9d**). In this context, we denoted that rRV/wt viroplasms  
326 were sensitive to jasp and cyt B treatment, as the ratio of cells showing viroplasms (**Fig 9e**)  
327 and the number of viroplasms per cell (**Fig 9f**) were significantly decreased, reaching the  
328 levels observed in rRV/VP<sub>4</sub>-BAP infected cells in presence or absence of actin inhibitors.

329 We next inhibited the non-muscular myosin II using blebbistatin (BLB)(63), a small  
330 molecule inhibiting both myosin II paralogs a and b (**Fig 9g-i**). Like the actin inhibitors,  
331 blebbistatin reduced the ratio of cells with viroplasms (**Fig 9h**) and the number of  
332 viroplasms per cell (**Fig 9i**) in cells infected with rRV/wt but not with rRV/VP<sub>4</sub>-BAP. Our  
333 results suggest that viroplasm assembly requires actin and myosin II in a mechanism  
334 employing VP<sub>4</sub>.

335 **A small peptide mimicking loop K145-G150 rescues the rRV/VP<sub>4</sub>-BAP phenotype.** It has  
336 been described that the C-terminal region of VP<sub>5</sub>\* harbors an actin-binding domain (45).  
337 We hypothesize that the insertion of a BAP tag in loop K145-G150 interferes with the  
338 association of VP<sub>5</sub>\* with the actin cytoskeleton, which results in a delay in viroplasm  
339 assembly because of an inability to reorganize the actin cytoskeleton. To prove this  
340 hypothesis, we designed a small peptide harboring the amino acid sequence of wt VP<sub>4</sub> loop  
341 K145-G150 flanked at the N-terminus by an arginine-tail and at the C-terminus by  
342 conjugation to fluorescein isothiocyanate (FITC), for peptidic internalization and  
343 visualization, respectively. Thus, the sequence of this small peptide corresponds to  
344 RRRRRR<sup>143</sup>VV<sup>145</sup>KTTANG<sup>150</sup>SIGQYG<sup>156</sup>-FITC, and was designated small peptide loop K145-  
345 G150 (SPL). Of note, SPL was not toxic for cells up to a concentration of 100 μM even after

346 24 h of treatment (**Fig S4a**). SPL was internalized in cells at 2 h post-treatment and found  
347 diffuse in the cytosol (**Fig S4b**). In the first instance (**Fig 10a**), we expressed VP<sub>4</sub>-GFP and  
348 VP<sub>4</sub>-BAP-GFP (stained with anti-GFP, red) in BHK-T<sub>7</sub> cells in the absence or presence of  
349 SPL and monitored the filamentous distribution of these proteins. Interestingly, as  
350 quantified in **Fig 10b**, the addition of SPL increased the length of VP<sub>4</sub>-BAP-GFP filaments  
351 compared to the untreated sample reaching the same level of the fiber lengths as VP<sub>4</sub>-GFP.  
352 The filamentous distribution of VP<sub>4</sub>-GFP did not change with SPL treatment. We next  
353 interrogated if SPL can improve the replication fitness of rRV/VP<sub>4</sub>-BAP. For this, SPL was  
354 added at 1 or 3 hpi to MA104 cells infected with either rRV/wt or rRV/VP<sub>4</sub>-BAP and then  
355 monitored at 6 hpi for viroplasm formation (**Fig 10c**). Surprisingly, the addition of SPL at 1  
356 hpi improved drastically the number of cells presenting viroplasms in rRV/VP<sub>4</sub>-BAP-  
357 infected cells, reaching similar levels as observed in rRV/wt infected cells (**Fig 10d**).  
358 Consistently, the viroplasm size and numbers per cell increased upon SPL treatment at 1  
359 hpi (**Fig 10e and f**). The addition of SPL at 3 hpi resulted in increased viroplasm size but not  
360 increased numbers per cell. The treatment of rRV/wt infected cells with SPL did not affect  
361 viroplasm size and numbers (**Fig S5c-d**). We then tested the ability of SPL to recover  
362 rRV/VP<sub>4</sub>-BAP virus progeny. For this purpose, rRV/VP<sub>4</sub>-BAP infected cells were treated at 1  
363 hpi with SPL, and virus progeny was recovered at 12 hpi. As denoted in **Fig 10g**, rRV/VP<sub>4</sub>-  
364 BAP virus progeny formation significantly increased upon treatment with SPL, while the  
365 same treatment had no effect on rRV/wt progeny formation. We concluded that SPL  
366 boosted the association of VP<sub>4</sub>-BAP to actin-bundles, thereby rescuing the assembly of  
367 viroplasms with a concomitant increase in the production of virus progeny.  
368



369 **Discussion**

370           The external coat layer of the RV virion can be modified *in vitro* by adding a specific  
371 ratio of VP7 and VP4 proteins to purified DLPs to generate recoated TLPs (rcTLPs) (10-12,  
372 64). This approach provides a valuable tool for studying the VP4 structural requirements for  
373 virion internalization (10). However, rcTLPs have methodological limitations and do not  
374 allow transferring the parental phenotype to the virus progeny. Moreover, rcTLPs only  
375 allow single amino acid substitutions in the VP4 spike protein (65, 66). However, the  
376 recently implemented entirely plasmid-based RV reverse genetics technology resulted in a  
377 valuable tool for studying several aspects of RV replication and the development of future  
378 RV based vaccines because it supports site-directed modifications of RV genome segments  
379 of interest. Specifically, RV reverse genetics technology has demonstrated that *gs4*,  
380 encoding VP4, can be artificially reassorted or recombined by transferring human RV strain  
381 *gs4* into a simian strain SA11 backbone (54).

382           In the present study, we used an RV reverse genetics system to remodel the spike  
383 protein VP4 by incorporating a BAP tag in four independent exposed loops in the VP8\*  
384 lectin domain. Interestingly, although the four differently modified proteins were efficiently  
385 biotinylated in transfected cells, only one of them harboring a BAP tag inserted in the K145-  
386 G150 loop, rRV/VP4-BAP, was rescued using RV reverse genetics (54). We hypothesize that  
387 those VP4-BAP versions, which were unable to be rescued, could have had strongly  
388 compromised their virus progeny because they directly impacted, and as denoted by *in*  
389 *silico* modeling of these structures (**Fig S5a**), *i*) the VP4 transition states from upright  
390 (immature) to reverse (mature) (65), *ii*) the VP4 association with specific cellular receptors  
391 (36, 37), or *iii*) the incorporation of VP4 in the coat layer.

392 VP<sub>4</sub>-BAP and VP<sub>4</sub> share similar distribution patterns in infected cells, such as their  
393 localization surrounding viroplasms, co-localization in the endoplasmic reticulum with VP<sub>7</sub>,  
394 and incorporation into newly assembled virions. However, we found that rRV/VP<sub>4</sub>-BAP had  
395 a significantly reduced replication fitness compared to rRV/wt. To identify the reason for  
396 this, we investigated the various steps involved in RV replication. We show that rRV/VP<sub>4</sub>-  
397 BAP internalization kinetics are comparable to those of the rRV/wt. This internalization  
398 kinetics consists of a sequence of events starting with the interaction of the virus with the  
399 cell membrane and concluding with the decrease of calcium levels within the endosomes,  
400 provoking the loss of the outer layer of the virion, which triggers the release of  
401 transcriptionally active DLPs into the cytosol (66-6g). We also confirmed that virus  
402 transcription and translation are comparable between both viruses. Moreover, there were  
403 no differences in rRV/VP<sub>4</sub>-BAP viroplasm morphology and liquid-like dynamics, as  
404 determined by high-resolution electron microscopy and NSP<sub>2</sub>-mCherry mobility on single-  
405 viroplasm FRAP experiments, respectively. However, upon transfection with rRV/VP<sub>4</sub>-BAP  
406 DLPs that bypass the virus physiological internalization pathway, showed a delayed  
407 viroplasm formation compared to rRV/wt DLPs, even though NSP<sub>5</sub> expression levels were  
408 equivalent for both viruses. Collectively, these results indicate that the reduced replication  
409 fitness of rRV/VP<sub>4</sub>-BAP is due to a step between primary virus translation and viroplasm  
410 formation. We hypothesize that rRV/VP<sub>4</sub>-BAP, and specifically VP<sub>4</sub>-BAP, was defective in  
411 associating with the actin cytoskeleton because we observed *i)* a delayed recovery of  
412 rRV/VP<sub>4</sub>-BAP viroplasms after 1,6-HD treatment, *ii)* inability of VP<sub>4</sub>-BAP-GFP to increase  
413 the VLS counts, *iii)* absence of co-localization of VP<sub>4</sub>-BAP-GFP with actin stress fibers, *iv)*  
414 inability of rRV/VP<sub>4</sub>-BAP to reorganize actin cytoskeleton, and *v)* insensitivity of rRV/VP<sub>4</sub>-  
415 BAP viroplasms for drugs depolymerizing actin filaments and inhibiting myosin II molecular

416 motor. In contrast, rRV/wt infection led to the reorganization of the actin cytoskeleton, and  
417 rRV/wt viroplasms were sensitive to actin-depolymerizing and myosin inhibitor drugs  
418 linking actin with viroplasm assembly. Additionally, the numbers of VLS duplicated when  
419 co-expressed with VP<sub>4</sub>-GFP. Previous studies (45, 49) demonstrated the ability of VP<sub>4</sub> to  
420 associate with actin in the absence of other virus proteins, mainly through an actin-binding  
421 domain present in the C-terminal region of VP<sub>5</sub>\* (residues 713-776) when in cooperation  
422 with the coiled-coil domain (residues 481-574). In this context, we also present evidence  
423 that the sole expression of VP<sub>4</sub> allows its association with actin. But importantly, by  
424 employing rRV/VP<sub>4</sub>-BAP infection, we show that the association of VP<sub>4</sub> with actin is  
425 essential to catalyze the formation of viroplasms. This finding provides an additional  
426 function to VP<sub>4</sub> in RV replication.

427         Interestingly, incorporating a small peptide mimicking loop K<sub>145</sub>-G<sub>150</sub> of VP<sub>4</sub>  
428 during rRV/VP<sub>4</sub>-BAP infection reverted the impaired formation of viroplasm with a  
429 significant improvement in virus progeny production. We concluded that rRV/VP<sub>4</sub>-BAP  
430 replication is enhanced because SPL raised the association of actin with VP<sub>4</sub>-BAP during  
431 virus infection and because we observed that VP<sub>4</sub>-BAP, in the absence of other viral  
432 proteins, associated with actin filament when expressed with SPL. We, therefore,  
433 hypothesize that the VP<sub>8</sub>\* subunit is involved in at least one of these three aspects that  
434 render the viroplasms assembled and stabilized: *i*) association of VP<sub>8</sub>\* with a yet  
435 undescribed host component, *ii*) a reorganization of VP<sub>5</sub>\*-VP<sub>8</sub>\* association or *iii*) a direct  
436 role of VP<sub>8</sub>\* over another RV protein in viroplasm assembly. The role of the actin  
437 cytoskeleton in the RV life cycle, particularly internalization and egress, has been previously  
438 demonstrated (39, 47, 70). Here, we show that the actin cytoskeleton is also involved in  
439 viroplasm formation, an essential intermediate stage of RV replication. It has been

440 described that the silencing of Rac1, a member of the Rho family of small GTPases playing  
441 a major role in actin- and microtubule-cytoskeleton dynamics, leads to a decrease in RV  
442 progeny formation in a process downstream of cell entry (70). We therefore cannot exclude  
443 activation of Rac1 by VP4, allowing reorganization of the actin cytoskeleton for an efficient  
444 assembly of the viroplasms.

445 Finally, specific *in vivo* biotinylation of cellular targets can be achieved by adding a  
446 BAP tag to the protein of interest and co-expressed with the *E.coli*-derived biotin ligase,  
447 BirA (71). This method is a powerful tool for versatile applications, such as identifying highly  
448 complex interactomes (72, 73), and permits batch protein and subviral particle (51, 52)  
449 refinement at high purity and in physiological conditions. The incorporation of a BAP tag in  
450 RV VP6, allowed the preparation and purification of replication-competent DLPs (52).  
451 Identifying a permissive target site in loop K145-G150 of VP4 spike protein for the insertion  
452 of an exogenous peptide may impact the RV field. This VP4 modification favors the  
453 insertion of peptides required for super-resolution microscopy or DNA-paint technologies  
454 (e.g., Halo or BC2 tags) to dissect debated aspects of RV entry. In addition, this VP4  
455 modification technology could permit the incorporation of antigenic peptides for vaccine  
456 development. Although it is well-known that the current oral RV vaccines elicit an efficient  
457 immune response (74, 75), rRV harboring a modified VP4 could provide an improved  
458 vaccination platform for the display of other antigens fostering the development of a new  
459 generation of dual vaccines.

460

## 461 **Material and Methods**

462 **Cells and viruses.** MA104 cells (embryonic African green monkey kidney cells; ATCC CRL-  
463 2378) were grown in Dulbecco's modified Eagle's medium (DMEM) (Life Technologies)

464 containing 10% fetal calf serum (FCS) (AMIMED; BioConcept, Switzerland) and penicillin  
465 (100 U/ml)-streptomycin (100 µg/ml) (Gibco, Life Technologies). MA/cytBirA and  
466 MA/NSP2-mCherry (59) cell lines were grown in DMEM supplemented with 10% FCS,  
467 penicillin (100 U/ml)-streptomycin (100 µg/ml) and 5 µg/ml puromycin (InvivoGen, France).  
468 BHK-T<sub>7/9</sub> (baby hamster kidney stably expressing T<sub>7</sub> RNA polymerase) cells were kindly  
469 provided by Naoto Ito (Gifu University, Japan)(76) and cultured in Glasgow medium  
470 supplemented with 5% FCS, 10% tryptose phosphate broth (Sigma-Aldrich), 10% FCS,  
471 penicillin(100 U/ml)-streptomycin (100 µg/ml), 2% nonessential amino acids and 1%  
472 glutamine.

473 rRV/wt (59), rRV/VP<sub>4</sub>-BAP, and simian rotavirus strain SA11 (G<sub>3</sub>P6[1])(77) were  
474 propagated, grown, and purified as previously described (78). Virus titer was determined as  
475 viroplasm forming units per ml (VFU/ml) as described by Eichwald et al. 2012 (25). The  
476 T<sub>7</sub> RNA polymerase recombinant vaccinia virus (strain vvT<sub>7.3</sub>) was amplified as previously  
477 described (79).

478 **Cell line generation.** MA/cyt-BirA cell line was generated using the PiggyBac technology  
479 (80). Briefly, 1x10<sup>5</sup> MA104 cells were transfected with the pCMV-HyPBBase (80) and  
480 transposon plasmids pPB-cytBirA using a ratio of 1:2.5 with Lipofectamine™ 3000  
481 transfection reagent (Invitrogen, Thermo Fisher Scientific) according to the manufacturer's  
482 instructions. The cells were maintained in DMEM supplemented with 10% FCS for  
483 three days and then selected for four days in DMEM supplemented with 10% FCS and  
484 5 µg/ml puromycin (59).

485 **Reverse genetics.** rRV/VP<sub>4</sub>-BAP was prepared as described previously (59, 81) using a pT<sub>7</sub>-  
486 VP<sub>4</sub>-BAP instead of pT<sub>7</sub>-VP<sub>4</sub>. Briefly, monolayers of BHK-T<sub>7</sub> cells (4x10<sup>5</sup>) cultured in 12-well  
487 plates were co-transfected using 2.5 µl of TransIT-LT1 transfection reagent (Mirus) per

488 microgram of DNA plasmid. The mixture comprised 0.8 µg of SA11 rescue plasmids: pT<sub>7</sub>-  
489 VP1, pT<sub>7</sub>-VP2, pT<sub>7</sub>-VP3, pT<sub>7</sub>-VP4-BAP, pT<sub>7</sub>-VP6, pT<sub>7</sub>-VP7, pT<sub>7</sub>-NSP1, pT<sub>7</sub>-NSP3, pT<sub>7</sub>-NSP4,  
490 and 2.4 µg of pT<sub>7</sub>-NSP2 and pT<sub>7</sub>-NSP5 (82, 83). Additionally, 0.8 µg of pcDNA3-NSP2 and  
491 0.8 µg of pcDNA3-NSP5, encoding NSP2 and NSP5 proteins, were co-transfected to  
492 increase rescue efficiency (59, 81). Next, cells were co-cultured with MA104 cells for three  
493 days in serum-free DMEM supplemented with trypsin from porcine pancreas (0.5 µg/ml  
494 final concentration) (To303-Sigma Aldrich) and lysed by freeze-thawing. Then, 300 µl of the  
495 lysate was transferred to new MA104 cells and cultured at 37°C for four days in serum-free  
496 DMEM supplemented with 0.5 µg/ml trypsin until a visible cytopathic effect was observed.  
497 The modified genome segments of rescued recombinant rotaviruses were confirmed by  
498 specific PCR segment amplification followed by sequencing (59).

499 **Antibodies and Chemicals.** Guinea pig anti-NSP5, guinea pig anti-RV, goat anti-RV, mouse  
500 monoclonal anti-NSP5 (clone 2D2), and rabbit anti-VP4 were described previously (25, 84-  
501 87). Mouse monoclonal anti-VP5 (clone 2G4) and mouse monoclonal anti-VP7 (clone 159)  
502 was kindly provided by Harry Greenberg (Stanford University, CA, USA). Rabbit anti-simian  
503 rotavirus VP4 was purchased from Abcam. Mouse mAb anti-glyceraldehyde  
504 dehydrogenase (GAPDH) (clone GAPDH-71.1), mouse anti-alpha tubulin (clone B-5-1-12),  
505 and mouse mAb anti-β-actin (clone AC-74) were purchased to Merck. Mouse mAb anti-GFP  
506 clone C-2) was purchased from Santa Cruz Biotechnology, Inc. Mouse mAb anti-α-tubulin  
507 was directly conjugated to Atto 488 using lightning-link™ Atto 488 conjugation kit from  
508 Innova Bioscience, UK. Streptavidin-HRP was purchased from Merck. Streptavidin-Alexa  
509 555 and secondary antibodies conjugated to Alexa 488, Alexa 594, Alexa 647, Alexa 700  
510 (ThermoFisher Scientific).

511 1,6-hexanediol, nocodazole, jasplakinolide, and cytochalasin B were purchased from  
512 Merck. (-)-Blesbbistatin was purchased from Cayman Chemical, USA.  
513 Amino acids and their derivatives were purchased from Advanced ChemTech,  
514 Novabiochem, Iris Biotech GMBH, Sigma-Aldrich, PolyPeptide, Space peptides and GL  
515 BioChem. Amino acids were used as the following derivatives Fmoc-Arg(Pbf)-OH, Fmoc-  
516 Leu-OH, Fmoc-Lys(Boc)-OH, Fmoc-Lys(Fmoc)-OH, Fmoc-Pro-OH, Fmoc-Val-OH, Fmoc-  
517 Trp(Boc)-OH, Fmoc-Ile-OH, Fmoc-Gln(Trt)-OH, Fmoc-Tyr(tBu)-OH, Fmoc-Ala-OH and Rink  
518 Amide AM resin (loading: 0.38 mmol·g<sup>-1</sup>) and were purchased from Sigma Aldrich.  
519 OxymaPure (hydroxyiminocyanoacetic acid ethyl ester) and DIC (*N,N'*-diisopropyl  
520 carbodiimide) were purchased from Iris Biotech GMBH. 5(6)-carboxyfluorescein (CF) was  
521 from Sigma. EM104 10ml glass syringes from Sanitex international.

522

523 **DNA plasmids.** pcDNA-VP<sub>4</sub>-SA<sub>11</sub> was obtained by RT-PCR amplification of VP<sub>4</sub> ORF of  
524 gs<sub>4</sub> of simian rotavirus strain SA<sub>11</sub> (88) using specific primers to insert *Hind*III and *Xho*I  
525 sites, followed by ligation into those sites in pcDNA<sub>3</sub> (Invitrogen). pcDNA-VP<sub>4</sub>-*Kpn*I/*Bam*HI  
526 was built by insertion of point mutations in pcDNA-VP<sub>4</sub>-SA<sub>11</sub> using the QuikChange site-  
527 directed mutagenesis kit and protocol (Agilent) to insert *Kpn*I and *Bam*HI restriction sites in  
528 VP<sub>4</sub>. pcDNA-VP<sub>4</sub>-BAP (blue), (orange), (pink), and (green) were obtained by ligation  
529 between *Kpn*I and *Bam*HI of pcDNA-VP<sub>4</sub>-*Kpn*I/*Bam*HI, a synthetic DNA fragment  
530 (GenScript®) containing BAP tag in VP<sub>4</sub> loops in amino acid regions 96-101, 109-114, 132-  
531 137 and 145-150, respectively. The BAP tags are flanked by *Bsp*EI and *Nhe*I restriction sites  
532 for easy tag replacement.

533 RV plasmids pT<sub>7</sub>-VP<sub>1</sub>-SA<sub>11</sub>, pT<sub>7</sub>-VP<sub>2</sub>-SA<sub>11</sub>, pT<sub>7</sub>-VP<sub>3</sub>-SA<sub>11</sub>, pT<sub>7</sub>-VP<sub>4</sub>-SA<sub>11</sub>, pT<sub>7</sub>-VP<sub>6</sub>-  
534 SA<sub>11</sub>, pT<sub>7</sub>-VP<sub>7</sub>-SA<sub>11</sub>, pT<sub>7</sub>-NSP<sub>1</sub>-SA<sub>11</sub>, pT<sub>7</sub>-NSP<sub>2</sub>-SA<sub>11</sub>, pT<sub>7</sub>-NSP<sub>3</sub>-SA<sub>11</sub>, pT<sub>7</sub>-NSP<sub>4</sub>-SA<sub>11</sub>,

535 and pT<sub>7</sub>-NSP5-SA<sub>11</sub> were previously described (82). pcDNA<sub>3</sub>-NSP<sub>5</sub> and pcDNA<sub>3</sub>-NSP<sub>2</sub>  
536 were already described (59). pT<sub>7</sub>-VP<sub>4</sub>-BAP (blue), (orange), (green), and (pink) were  
537 obtained by inserting a synthetic DNA fragment (Genscript) encoding for the VP<sub>4</sub> protein-  
538 encoding BAP tag flanked by *MfeI* and *NdeI* restriction enzymes sites and ligated into those  
539 sites in the pT<sub>7</sub>-VP<sub>4</sub>-SA<sub>11</sub>.

540 pPB-cytBirA was obtained from a synthetic DNA fragment (Genscript) containing  
541 the BirA enzyme open reading frame of *Escherichia coli* (UniProt accession number:  
542 P06709) and inserted in the pPB-MCS vector (81) using *NheI*-*BamHI* restriction enzymes  
543 sites.

544 pcDNA-NSP<sub>5</sub>(SA<sub>11</sub>) and pcDNA-NSP<sub>2</sub>(SA<sub>11</sub>) were previously described (24, 89).  
545 pCI-VP<sub>4</sub>-GFP and pCI-VP<sub>4</sub>-BAP plasmids were obtained from PCR amplification of pT<sub>7</sub>-  
546 VP<sub>4</sub>-SA<sub>11</sub> and pT<sub>7</sub>-VP<sub>4</sub>-BAP (green) using specific primers to insert *NheI* and *MluI* sites,  
547 followed by ligation in-frame on those sites in pCI-GFP. Thus, the GFP fragment was PCR  
548 amplified from pEGFP-N<sub>1</sub> (Clontech) using specific primers to insert *MluI*/*NotI* restriction  
549 enzyme sites and ligated on those restriction enzyme sites into pCI-Neo (Promega). All the  
550 oligonucleotides were obtained from Microsynth AG, Switzerland. A list of all DNA  
551 sequences synthesized is provided in **Table S1**.

552 **Streptavidin-supershift assay and immunoblotting.** The assay was performed as  
553 described by Predonzani et al (51). Briefly, cell extracts were lysed in TNN lysis buffer  
554 (100mM Tri-HCl pH8.0, 250 mM NaCl, 0.5% NP-40, and cOmplete protease inhibitor  
555 (Roche)) and centrifuged for 7 min at 15'000 rpm and 4°C. The supernatant was  
556 exhaustively dialyzed against PBS (phosphate-buffered saline, 137 mM NaCl, 2.7 mM KCl, 8  
557 mM Na<sub>2</sub>HPO<sub>4</sub>, and 2 mM KH<sub>2</sub>PO<sub>4</sub> pH 7.2) at 4°C and heated for 5 min at 95°C in Laemmli  
558 sample buffer. Samples were incubated for 1 h at 4°C with 1 µg streptavidin (Sigma) and



559 then resolved in SDS-polyacrylamide gel under reducing conditions. Proteins were  
560 transferred to nitrocellulose 0.45  $\mu\text{m}$  (90) and incubated with corresponding primary and  
561 secondary antibodies. Secondary antibodies were conjugated to IRDye680RD or  
562 IRDye800RD (LI-COR, Germany) for protein detection and quantification in Odyssey® Fc  
563 (LI-COR Biosciences).

564 **Virus fitness curve.** The experiment was performed as described previously (91) with some  
565 modifications. MA104 cells ( $1 \times 10^5$ ) seeded in 24-well plates were infected with rRV at an  
566 MOI of 10 VFU/cell. The virus was allowed to adsorb for 1 h at 4°C, followed by incubation  
567 at 37°C in 500  $\mu\text{l}$  DMEM. At the indicated time points, the plates were frozen at -80°C. Each  
568 time point was performed in triplicated. The cells were freeze-thawed for three cycles,  
569 harvested, and centrifuged at  $900 \times g$  for 5 min at 4°C. The supernatant was recovered and  
570 activated with 80  $\mu\text{g}/\text{ml}$  of trypsin for 30 min at 37°C. Two-fold serial dilutions were  
571 prepared and used to determine the viral titers described previously (59, 81).

572 **Fluorescence labeling of purified rRV.** 100  $\mu\text{l}$  of purified and trypsin activated biotinylated  
573 rRV/VP<sub>4</sub>-BAP was incubated with 1  $\mu\text{l}$  of streptavidin-Alexa Fluor 555 (2mg/ml)  
574 (ThermoFisher Scientific) for 1 h at room temperature. The tube was snapped every 20 min.  
575 Unbound streptavidin and streptavidin conjugated to rRV/VP<sub>4</sub>-BAP were separated by  
576 loading the 50  $\mu\text{l}$  reaction mixture on top of 100  $\mu\text{l}$  of a 20% sucrose-PBS cushion followed  
577 by centrifugation for 40 min at 20 psi in an air-driven ultracentrifuge (Airfuge, Beckman  
578 Coulter). Pellet was resuspended in 20  $\mu\text{l}$  TBS (25 mM Tris-HCl, pH 7.4, 137 mM NaCl, 5 mM  
579 KCl, 1 mM MgCl<sub>2</sub>, 0.7 mM CaCl<sub>2</sub>, 0.7 mM Na<sub>2</sub>HPO<sub>4</sub>, 5.5 mM dextrose).

580 **Immunofluorescence.** For virus internalization experiments, 1  $\mu\text{l}$  of rRV particles  
581 conjugated to StAV-Alexa555 diluted in 50  $\mu\text{l}$  of DMEM was adsorbed over MA104 cells for

582 15 min and kept on a metal tray cooled to -20°C. Cells were then transferred to 37°C and  
583 fixed at the indicated time-points with ice-cold methanol for 3 min on dry ice.

584 For later times post-infection, the virus was adsorbed for 1 h at 4°C in a reduced  
585 volume. Then, cells were transferred to 37°C and treated at the indicated time points with  
586 100 µM biotin in serum-free DMEM. Cells were fixed when indicated in 2%  
587 paraformaldehyde in phosphate-buffered saline (PBS) for 10 min at room temperature or  
588 in ice cold-methanol for 3 min at -20°C.

589 VLS experiments were performed as described by Buttafuoco *et al.* (90). In  
590 experiments using the inhibitors, the drug was added at 1 hpi and maintained until 6 hpi.  
591 The concentrations used 0.5 µM jasplakinolide (61, 70), 10 µM cytochalasin B (92) and 5 µM  
592 blebbistatin (63) were described elsewhere.

593 All immunofluorescence assays were processed as described by Buttafuoco *et al.* (90).  
594 Images were acquired using a confocal laser scanning microscope (CLSM) (DM550Q; Leica).  
595 Data were analyzed with the Leica Application Suite (Mannheim, Germany) and Image J  
596 (93).

597 **LLPS assay.** MA/NSP2-mCherry cells were seeded at a density of  $1.2 \times 10^4$  cells per well 8-  
598 wells Lab-Tek® Chamber Slide™ (Nunc, Inc. Cat #177402). For RV infection, the virus was  
599 adsorbed at MOI of 25 VFU/cell diluted in 30 µl of serum-free DMEM, incubated at 4°C for 1  
600 h in an orbital shaker, and then volume filled to 100µl with serum-free DMEM followed by  
601 incubation at 37°C. At 5 hpi, the medium was replaced by medium containing 3.5% 1,6-  
602 hexanediol in 2% FCS-DMEM and cells were incubated for 6 min at 37°C. Then the drug was  
603 washed out by removing the medium, washing the cells three times with PBS, adding fresh  
604 2% FCS-DMEM, and incubating at 37°C. At the designated time post-recovery, cells were  
605 fixed with 2% PFA for 10 min at room temperature. Finally, nuclei were stained by

606 incubating cells with 1 µg/ml of DAPI (4',6-diamidino-2-phenylindole) in PBS for 15 min at  
607 room temperature. Samples were mounted in ProLong™ Gold antifade mountant  
608 (ThermoFisher Scientific), and images were acquired using a fluorescence microscope  
609 (DMI6000B, Leica). Data were analyzed using ImageJ software (version 2.1.0/1.53;  
610 <https://imagej.net/Fiji>).

611 **Quantification of viroplasm.** The number of viroplasms was acquired and analyzed as  
612 previously described (25, 61, 92). Data analysis was performed using Microsoft® Excel for  
613 Mac version 16.58. Statistical analysis, unpaired parametric Welch's t-test comparison post-  
614 test, and plots were performed using Prism 9 for macOS version 9.3.1 (GraphPad Software,  
615 LLC).

616 **Rotavirus electropherotype.** Rotavirus genome extraction and visualization were  
617 performed as previously described (94). Briefly, MA104 cells at a density of  $3 \times 10^5$  cells per  
618 well in a 6-well multiwell plate were infected with a virus at MOI of 10 VFU/cell and  
619 incubated in 1 ml serum free DMEM until complete cytopathic effect was reached. The cells  
620 and supernatant were harvested, followed by three cycles of liquid nitrogen freeze and 37°C  
621 water bath. Then, the samples were mixed vigorously at a ratio of 1:1 with saturated phenol  
622 solution pH 4.3 (Merck) and centrifuged for 15 min at 13'000 rpm. The aqueous phase was  
623 recovered, and the previous step was repeated. Then, the RNA in the recovered aqueous  
624 phase was precipitated by mixing with 0.1 vol 3M Na Acetate at pH 5.2 and 2 vol of 100%  
625 ethanol. Samples were incubated for 30 min at -80°C and then centrifuged at 13'000 rpm  
626 for 30 min and 4°C. The pellet was resuspended in 15 µl distilled water and mixed with 10 µl  
627 Gel Loading dye 6X (New England BioLabs). The samples were migrated in an 8.5% SDS-  
628 polyacrylamide gel at 180 Volts for 120 min, followed by staining with GelRed® Acid gel  
629 Stain (Biotium) for 30 min. Images were acquired at Odyssey® FC (LI-COR Biosciences).

630 **Transmission electron microscopy.** MA104 cells were seeded at  $1 \times 10^5$  cells in a 2-cm<sup>2</sup> well  
631 onto sapphire discs and infected with either rRV/wt or rRV/VP<sub>4</sub>-BAP at an MOI of 50  
632 VFU/ml. At 6 and 12 hpi, the sapphire discs were collected, fixed with 2.5% glutaraldehyde  
633 in 100 mM Na/K-phosphate buffer, pH 7.4, for 1 h at 4°C and then kept in 100 mM Na/K-  
634 phosphate buffer overnight at 4°C. Afterward, samples were postfixed in 1% osmium  
635 tetroxide in 100 mM Na/K-phosphate buffer for 1 h at 4°C, dehydrated in a graded ethanol  
636 series starting at 70%, followed by two changes in acetone, and embedded in Epon.  
637 Ultrathin sections (60 to 80 nm) were cut and stained with uranyl acetate and lead citrate.

638 For staining biotinylated TLPs with streptavidin-gold, purified particles were  
639 dialyzed overnight at 4°C in TNC buffer (10 mM Tris-HCl, pH 7.5, 140 mM NaCl, 10mM  
640 CaCl<sub>2</sub>). The TLPs were adsorbed for 10 min on carbon-coated Parlodion films mounted on  
641 300-mesh copper grids (EMS). Samples were washed once with water, fixed in 2.5%  
642 glutaraldehyde in 100 mM Na/K-phosphate buffer, pH 7.0, for 10 min at room temperature,  
643 and washed twice with PBS before incubation for 2 h at room temperature with 10 µl  
644 streptavidin conjugated to 10 nm colloidal gold (Sigma-Aldrich, Inc). Before use, the  
645 streptavidin-gold conjugate was treated as described previously to separate unconjugated  
646 streptavidin from streptavidin-conjugated to colloidal gold (95). The viral particles were  
647 washed three times with water and stained with 2% phosphotungstate, pH 7.0, for 1 min at  
648 room temperature. Samples were analyzed in a transmission electron microscope (CM12;  
649 Philips, Eindhoven, The Netherlands) equipped with coupled device (CCD) cameras  
650 (Ultrascan 1000 and Orius SC1000A; Gatan, Pleasanton, CA, USA) at an acceleration  
651 voltage of 100 kV.

652 For calculation of the diameter of virus particles by negative staining, the area of each  
653 virus particle was calculated using Imaris software (version 2.1.0/1.53c; Creative Commons

654 license) and then converted to the diameter as follows:  $d = 2 \times \sqrt{A/\pi}$ , where A is the area  
655 and d is the diameter of the particle, respectively.

656 **siRNA reverse transfection.** For silencing gs<sub>4</sub> of SA<sub>11</sub> strain, the following siRNA pool:  
657 siVP<sub>4</sub>-25 (5'-uugcucacgaauucuuauatt-3'), siVP<sub>4</sub>-931 (5'-gaaguuaccgcacauacuatt-3') and  
658 siVP<sub>4</sub>-1534 (5'-auugcaaugucgcaguuatt-3') was designed and synthesized by Microsynth  
659 AG (Switzerland). siRNA-A (sc-37007, Santa Cruz Biotechnology) was used as negative  
660 siRNA control. siRNA reverse transfection was performed by mixing 1.2 µl siRNA 5 µM with  
661 1 µl lipofectamine RNAiMAX transfection reagent (Invitrogen, ThermoFisher Scientific) to a  
662 final volume of 100 µl with Opti-MEM® (Gibco, ThermoFisher Scientific) in a well of 24-well  
663 plate and incubated for 20 min at room temperature. To reach a 10 nM siRNA final  
664 concentration, 2 × 10<sup>4</sup> cells diluted in 500 µl DMEM supplemented with 10% FCS were  
665 added on top. Samples were incubated for 60 h prior to analysis. Thus, cells were infected  
666 with simian RV strain SA<sub>11</sub> at MOI 12 VFU/cell as described previously (25, 90, 91).

667 **FRAP.** 1.2 × 10<sup>4</sup> MA/NSP<sub>2</sub> cells per well were seeded in µ-Slide 18-well glass-bottom plates  
668 (Ibidi). Cells were RV-infected at MOI of 15 VFU/cell and kept in DMEM-SF. At 4.5 hpi, the  
669 cells were counterstained with Hoechst 33342 diluted in FluoroBRITE DMEM (Gibco,  
670 Cat.No. A18967-01) at a concentration of 1 µg/ml, incubated for 30 min at 37°C, and  
671 subjected to FRAP analysis. FRAP experiments were performed with an SP8 Falcon  
672 confocal laser scanning microscope (CLSM) from Leica equipped with a 63x objective (NA  
673 1.4) using the FRAP function of the LasX software (Leica) as follows: a circular area of 2 µm  
674 in diameter, encompassing an entire viroplasm, was bleached with the 405 nm and 481 nm  
675 lasers simultaneously, each at 100% laser power, for 20 iterations. The fluorescent recovery  
676 was monitored by taking fluorescence images of the mCherry channel every 2 seconds for

677 140 seconds. For each FRAP acquisition, a circular area of 2  $\mu\text{m}$ , encompassing an entire  
678 unbleached viroplasm in the same cell, was used as the fluorescent control, and a squared  
679 area (5  $\mu\text{m}$  x 5  $\mu\text{m}$ ) outside of a cell was chosen as the background. The entire FRAP dataset  
680 was analyzed with MatLab (MATLAB R2020b, Mathworks) using the FRAP-tool source  
681 code from easyFRAP (Cell Cycle Lab, Medical School, University of Patras). Fully  
682 normalized data were used to generate FRAP diagrams and calculate the recovery half-  
683 times (T-half) and mobile fractions from independent measurements. Representative  
684 images were taken and processed for each FRAP experiment using the Imaris software v9.5  
685 (Bitplane, Oxford Instruments). Fluorescent intensities of FRAP movies were normalized  
686 using a customized Fiji pipeline (93).

687 **Quantitative RT-PCR.** MA104 cells at a density of  $5 \times 10^5$  cells per well in 6 well multiwell  
688 plates were RV-infected at an MOI of 18 VFU/cell. The virus was adsorbed for 1 h at 4°C. At  
689 4 hpi, RNA was extracted using a quick RNA miniprepPlus kit (Zymo Research) according to  
690 the manufacturer's instructions. cDNA synthesis was prepared with 1  $\mu\text{g}$  of RNA using an  
691 AMV reverse transcription system (Promega) and random primers according to the  
692 manufacturer's instructions. Then 2  $\mu\text{l}$  of 1:10 diluted cDNA was mixed with 0.25  $\mu\text{l}$  forward  
693 primer (10 pmol/ $\mu\text{l}$ ), 0.25  $\mu\text{l}$  reverse primer (10 pmol/ $\mu\text{l}$ ) (**Supplementary Table 2**), 10  $\mu\text{l}$   
694 SYBR<sup>TM</sup> Green PCR master mix (Applied biosystems), and 7.5  $\mu\text{l}$  nuclease-free water  
695 followed by incubation at QuantStudio3 (Applied Biosystems, ThermoFisher Scientific)  
696 using standard amplification protocol with an annealing temperature of 60 °C. The relative  
697 expression of genes was calculated with the formula  $2^{-\Delta\text{Ct}}$ , where  $\Delta\text{Ct} = \text{Ct target gene} - \text{Ct}$   
698 endogenous control gene. HPRT-1, SDHA and GAPDH were used as an endogenous control  
699 housekeeping gene. Data were analyzed using Microsoft Excel for MAC (version 16.58).

700 Statistical analysis and plots were done using Prism9 for macOS (version 9.3.1) (GraphPad  
701 Software, LLC).

702 **Purification and transfection of DLPs.** RV amount sufficient to infect  $1 \times 10^6$  cells at MOI  
703 of 15 VFU/cell was diluted up to 110  $\mu$ l with TBS. Then EDTA pH 8.0 was added to a final  
704 concentration of 10 mM. The samples were incubated for 1 h at 37°C with gentle mixing and  
705 centrifuged at 3000 rpm for 2 min. The supernatant was recovered, loaded on top of a 100  
706  $\mu$ l cushion composed of 20% sucrose in PBS, and ultracentrifuged at 20 psi for 60 min on an  
707 air-driven ultracentrifuge (Airfuge, Beckman Coulter). For quality control, DLPs were  
708 monitored by negative staining electron microscopy. The DLPs were normalized using  
709 Pierce™ Coomassie protein assay kit (ThermoFisher Scientific) to determine the amount of  
710 total protein followed by an indirect ELISA to normalize to rotavirus protein using as  
711 primary antibody a guinea pig anti-rotavirus, which detected mainly VP6. Thus, DLPs were  
712 transfected by diluting them in 12.5  $\mu$ l Opti-MEM and mixed with 0.75  $\mu$ l Lipofectamine  
713 2000 (Invitrogen) in 12.5  $\mu$ l Opti-MEM. The mixture was incubated for 20 min at room  
714 temperature and added onto  $1 \times 10^4$  MA104 cells per well in a 96-well black wall tissue  
715 culture plate (Greiner). At 6 hpi, cells were fixed with paraformaldehyde and prepared for  
716 immunofluorescence as described above. Images were acquired using a CLSM and then  
717 processed with Image J2 version 2.3.0/1.53f.

718 **In-cell western assay.** RV-infected MA104 cells ( $1 \times 10^4$ ) were seeded in a 96-well black  
719 tissue culture plate (Greiner). At indicated times post-infection, cells were fixed with 2%  
720 paraformaldehyde in PBS for 10 min at room temperature, followed by permeabilization  
721 with 0.1% triton X-100-PBS for 10 min at room temperature. Cells were blocked with 2%  
722 BSA in PBS for 1 h at room temperature and then incubated with primary antibodies diluted

723 in blocking buffer for 1 h at room temperature in the shaker. The cells were incubated with  
724 the corresponding secondary antibody conjugated to IRDye® 800 CW (LI-COR). The cell  
725 signal was normalized using CellTag™ 700 stain (LI-COR) diluted at 1:800. The cells were  
726 washed three times with 0.01% Tween 20 in PBS between incubations. Samples were  
727 acquired using an Odyssey CLx (LI-COR) followed by data analysis and normalization in  
728 Microsoft® Excel for Mac version 16.58. Statistical analysis, unpaired Student's t-test, and  
729 plots were performed using Prism 9 for macOS version 9.3.1 (GraphPad Software, LLC).

730 **Virus attachment assay.** Rotavirus binding was determined by a nonradioactive binding  
731 assay as described previously in detail by Zarate *et al.* (56). The plates were coated with  
732 goat anti-rotavirus (diluted 1:5000) to capture the virus. In addition, guinea pig anti-  
733 rotavirus (diluted 1:5000) or streptavidin-HRP (diluted 1:500, Sigma) were used to detect  
734 the virus. The reaction was developed using 100 µl of Pierce TMB substrate kit  
735 (ThermoFisher) and stopped with 100 µl 1M H<sub>2</sub>SO<sub>4</sub>. Samples were recorded at an  
736 absorbance of 450 nm using an Infinite M Plex (Tecan) plate reader. Data analysis was  
737 performed using Microsoft® Excel for Mac version 16.58. Statistical analysis, semilog line  
738 nonlinear regression, and plots were performed using Prism 9 for macOS version 9.3.1  
739 (GraphPad Software, LLC).

740 **Linear peptide synthesis.** The linear peptide was synthesized using an automated peptide  
741 synthesis system developed in our laboratory. In here, 200 mg of resin was swelled in 6 ml  
742 100% dimethylformamide (DMF) for 5 min at 60 °C with nitrogen bubbling using a Teflon  
743 tube of 1/8-inch inner diameter. Importantly, the bubbling with nitrogen is kept during the  
744 entire synthesis process. The Fmoc-protecting groups of the resin were removed by  
745 washing twice with 6 ml solution of 20 % piperidine in DMF. For the first deprotection, the



746 sample was incubated for 1 min at 60 °C followed by aspiration. The second deprotection  
747 was obtained by incubating for 4 min at 60 °C followed by four washes with 7 ml DMF. The  
748 coupling of amino acids to unprotected resin or to the subsequent unprotected amino acids  
749 in the elongated peptide coupled to the resin was performed by adding twice 7.5 ml  
750 mixture of respective amino acid (5 eq/amine – 3 ml of 200mM), OxymaPure (7.5 eq./amine  
751 – 2ml of) and DIC (10 eq./amine – 2.5ml of) dissolved in DMF. The amino acids were coupled  
752 for two times 8 min at 60 °C with two times with 7 ml DMF wash after the first coupling and  
753 three times with 7 ml DMF wash after the second coupling. After each coupling, the newly  
754 bound amino acid was deprotected as mentioned above. The coupling reaction time was  
755 specifically extended to 10 min for Asp, Glu and Arg and temperature was lowered to 50 °C  
756 for Asp and Glu. The final deprotection was performed in the same manner as explained  
757 above. The newly synthesized peptide was washed twice with methanol and dried under  
758 vacuum. The peptide cleavage was carried out using TFA/TIS/H<sub>2</sub>O (94:5:1 v/v/v) for 4 h in 10  
759 ml plastic syringe mounted on a rotter. Then, the peptide was collected in 50 ml tubes,  
760 initially with gravity flow and subsequently, by inserting the plunger into the syringe. After  
761 filtration, the peptide was precipitated with 50 ml ice cold tert-butylmethylether (TBME),  
762 centrifuged at 4400 rpm for 15 min, and washed twice with TBME. For purification of the  
763 crude peptide, it was dissolved in 10 ml of a solution containing 100% mQ-H<sub>2</sub>O, 0.1% TFA,  
764 subjected to preparative RP-HPLC and obtained as TFA salt after lyophilisation. MS spectra  
765 were provided by Mass Spectrometry of the Department of Chemistry and Biochemistry at  
766 the University of Bern.

767

768 **Acknowledgments**

769 We thank Jakub Kubacki for his support of deep sequencing technology. This work has  
770 been supported by the University of Zurich. A pre-doctoral ICGEB fellowship also supported  
771 this project for GP and GDL. KG was supported by Diaconis-AMM Berner Stellennetz,  
772 Switzerland.

773 The authors declare no conflict of interest.

## 774 **References**

- 775 1. Troeger C, Khalil IA, Rao PC, Cao S, Blacker BF, Ahmed T, Armah G, Bines JE,  
776 Brewer TG, Colombara DV, Kang G, Kirkpatrick BD, Kirkwood CD, Mwenda JM,  
777 Parashar UD, Petri WA, Riddle MS, Steele AD, Thompson RL, Walson JL, Sanders  
778 JW, Mokdad AH, Murray CJL, Hay SI, Reiner RC. 2018. Rotavirus vaccination and the  
779 global burden of rotavirus diarrhea among children younger than 5 years. *JAMA*  
780 *Pediatr* 172:958-965.
- 781 2. Gomez DE, Weese JS. 2017. Viral enteritis in calves. *Can Vet J* 58:1267-1274.
- 782 3. Vlasova AN, Amimo JO, Saif LJ. 2017. Porcine rotaviruses: epidemiology, immune  
783 responses and control strategies. *Viruses* 9.
- 784 4. Dhama K, Saminathan M, Karthik K, Tiwari R, Shabbir MZ, Kumar N, Malik YS,  
785 Singh RK. 2015. Avian rotavirus enteritis - an updated review. *Vet Q* 35:142-58.
- 786 5. Lawton JA, Zeng CQ, Mukherjee SK, Cohen J, Estes MK, Prasad BV. 1997. Three-  
787 dimensional structural analysis of recombinant rotavirus-like particles with intact  
788 and amino-terminal-deleted VP2: implications for the architecture of the VP2 capsid  
789 layer. *J Virol* 71:7353-60.
- 790 6. Zhang X, Settembre E, Xu C, Dormitzer PR, Bellamy R, Harrison SC, Grigorieff N.  
791 2008. Near-atomic resolution using electron cryomicroscopy and single-particle  
792 reconstruction. *Proc Natl Acad Sci U S A* 105:1867-72.
- 793 7. Charpilienne A, Lepault J, Rey F, Cohen J. 2002. Identification of rotavirus VP6  
794 residues located at the interface with VP2 that are essential for capsid assembly and  
795 transcriptase activity. *J Virol* 76:7822-31.
- 796 8. Lepault J, Petitpas I, Erk I, Navaza J, Bigot D, Dona M, Vachette P, Cohen J, Rey FA.  
797 2001. Structural polymorphism of the major capsid protein of rotavirus. *EMBO J*  
798 20:1498-507.
- 799 9. Li Z, Baker ML, Jiang W, Estes MK, Prasad BV. 2009. Rotavirus architecture at  
800 subnanometer resolution. *J Virol* 83:1754-66.
- 801 10. Settembre EC, Chen JZ, Dormitzer PR, Grigorieff N, Harrison SC. 2011. Atomic  
802 model of an infectious rotavirus particle. *EMBO J* 30:408-16.

- 803 11. Yoder JD, Dormitzer PR. 2006. Alternative intermolecular contacts underlie the  
804 rotavirus VP5\* two- to three-fold rearrangement. *EMBO J* 25:1559-68.
- 805 12. Yoder JD, Trask SD, Vo TP, Binka M, Feng N, Harrison SC, Greenberg HB, Dormitzer  
806 PR. 2009. VP5\* rearranges when rotavirus uncoats. *J Virol* 83:11372-7.
- 807 13. Arias Carlos F, Silva-Ayala D, López S, Tsai B. Rotavirus entry: a deep journey into  
808 the cell with several exits. *J Virol* 89:890-893.
- 809 14. Deo RC, Groft CM, Rajashankar KR, Burley SK. 2002. Recognition of the rotavirus  
810 mRNA 3' consensus by an asymmetric NSP3 homodimer. *cell* 108:71-81.
- 811 15. Groft CM, Burley SK. 2002. Recognition of eIF4G by rotavirus NSP3 reveals a basis  
812 for mRNA circularization. *Molecular cell* 9:1273-1283.
- 813 16. López S, Arias CF. 2012. Rotavirus–host cell interactions: an arms race. *Current*  
814 *Opinion in Virology* 2:389-398.
- 815 17. Montero H, Arias CF, Lopez S. 2006. Rotavirus nonstructural protein NSP3 is not  
816 required for viral protein synthesis. *J Virol* 80:9031-8.
- 817 18. Piron M, Vende P, Cohen J, Poncet D. 1998. Rotavirus RNA-binding protein NSP3  
818 interacts with eIF4GI and evicts the poly (A) binding protein from eIF4F. *The EMBO*  
819 *journal* 17:5811-5821.
- 820 19. Barro M, Patton JT. 2005. Rotavirus nonstructural protein 1 subverts innate immune  
821 response by inducing degradation of IFN regulatory factor 3. *Proc Natl Acad Sci U S*  
822 *A* 102:4114-4119.
- 823 20. Patton JT, Silvestri LS, Tortorici MA, Carpio V-D, Taraporewala ZF. 2006. Rotavirus  
824 genome replication and morphogenesis: role of the viroplasm. *Reoviruses: entry,*  
825 *assembly and morphogenesis:169-187.*
- 826 21. Eichwald C, Rodriguez JF, Burrone OR. 2004. Characterization of rotavirus  
827 NSP2/NSP5 interactions and the dynamics of viroplasm formation. *J Gen Virol*  
828 85:625-34.
- 829 22. Contin R, Arnoldi F, Campagna M, Burrone OR. 2010. Rotavirus NSP5 orchestrates  
830 recruitment of viroplasmic proteins. *J Gen Virol* 91:1782-93.
- 831 23. Papa G, Borodavka A, Desselberger U. 2021. Viroplasms: assembly and functions of  
832 rotavirus replication factories. *Viruses* 13:1349.
- 833 24. Fabbretti E, Afrikanova I, Vascotto F, Burrone OR. 1999. Two non-structural  
834 rotavirus proteins, NSP2 and NSP5, form viroplasm-like structures *in vivo*. *J Gen*  
835 *Virol* 80 ( Pt 2):333-9.
- 836 25. Eichwald C, Arnoldi F, Laimbacher AS, Schraner EM, Fraefel C, Wild P, Burrone OR,  
837 Ackermann M. 2012. Rotavirus viroplasm fusion and perinuclear localization are  
838 dynamic processes requiring stabilized microtubules. *PLoS One* 7:e47947.

- 839 26. Cheung W, Gill M, Esposito A, Kaminski CF, Courousse N, Chwetzoff S, Trugnan G,  
840 Keshavan N, Lever A, Desselberger U. 2010. Rotaviruses associate with cellular lipid  
841 droplet components to replicate in viroplasms, and compounds disrupting or  
842 blocking lipid droplets inhibit viroplasm formation and viral replication. *J Virol*  
843 84:6782-6798.
- 844 27. Zhou Y, Chen L, Du J, Hu X, Xie Y, Wu J, Lin X, Yin N, Sun M, Li H. 2020. MicroRNA-7  
845 inhibits rotavirus replication by targeting viral NSP5 *in vivo* and *in vitro*. *Viruses* 12.
- 846 28. Geiger F, Acker J, Papa G, Wang X, Arter WE, Saar KL, Erkamp NA, Qi R, Bravo JPK,  
847 Strauss S, Krainer G, Burrone OR, Jungmann R, Knowles TPJ, Engelke H, Borodavka  
848 A. 2021. Liquid-liquid phase separation underpins the formation of replication  
849 factories in rotaviruses. *The EMBO Journal* 40:e107711.
- 850 29. Zambrano JL, Sorondo O, Alcala A, Vizzi E, Diaz Y, Ruiz MC, Michelangeli F,  
851 Liprandi F, Ludert JE. 2012. Rotavirus infection of cells in culture induces activation  
852 of RhoA and changes in the actin and tubulin cytoskeleton. *PLoS One* 7:e47612.
- 853 30. Trask SD, McDonald SM, Patton JT. 2012. Structural insights into the coupling of  
854 virion assembly and rotavirus replication. *Nat Rev Microbiol* 10:165-77.
- 855 31. Arias CF, Romero P, Alvarez V, López S. 1996. Trypsin activation pathway of  
856 rotavirus infectivity. *J Virol* 70:5832-9.
- 857 32. Gilbert JM, Greenberg HB. 1998. Cleavage of rhesus rotavirus VP4 after arginine 247  
858 is essential for rotavirus-like particle-induced fusion from without. *J Virol* 72:5323-7.
- 859 33. Dormitzer PR, Nason EB, Prasad BV, Harrison SC. 2004. Structural rearrangements  
860 in the membrane penetration protein of a non-enveloped virus. *Nature* 430:1053-8.
- 861 34. Dormitzer PR, Sun ZY, Wagner G, Harrison SC. 2002. The rhesus rotavirus VP4 sialic  
862 acid binding domain has a galectin fold with a novel carbohydrate binding site.  
863 *EMBO J* 21:885-97.
- 864 35. Fiore L, Greenberg HB, Mackow ER. 1991. The VP8 fragment of VP4 is the rhesus  
865 rotavirus hemagglutinin. *Virology* 181:553-63.
- 866 36. Graham KL, Halasz P, Tan Y, Hewish MJ, Takada Y, Mackow ER, Robinson MK,  
867 Coulson BS. 2003. Integrin-using rotaviruses bind alpha2beta1 integrin alpha2 I  
868 domain via VP4 DGE sequence and recognize alphaXbeta2 and alphaVbeta3 by  
869 using VP7 during cell entry. *J Virol* 77:9969-78.
- 870 37. Graham KL, Takada Y, Coulson BS. 2006. Rotavirus spike protein VP5\* binds  
871 alpha2beta1 integrin on the cell surface and competes with virus for cell binding and  
872 infectivity. *J Gen Virol* 87:1275-1283.
- 873 38. Estes MK, Graham DY, Gerba CP, Smith EM. 1979. Simian rotavirus SA11 replication  
874 in cell cultures. *J Virol* 31:810-5.

- 875 39. Arias CF, López S. 2021. Rotavirus cell entry: not so simple after all. *Current Opinion*  
876 *in Virology* 48:42-48.
- 877 40. Díaz-Salinas MA, Romero P, Espinosa R, Hoshino Y, López S, Arias CF. 2013. The  
878 spike protein VP<sub>4</sub> defines the endocytic pathway used by rotavirus to enter MA104  
879 cells. *J Virol* 87:1658-1663.
- 880 41. Enouf V, Chwetzoff S, Trugnan G, Cohen J. 2003. Interactions of rotavirus VP<sub>4</sub> spike  
881 protein with the endosomal protein Rab5 and the prenylated Rab acceptor PRA1. *J*  
882 *Virol* 77:7041-7.
- 883 42. Zárate S, Cuadras MA, Espinosa R, Romero P, Juárez KO, Camacho-Nuez M, Arias  
884 CF, López S. 2003. Interaction of rotaviruses with Hsc70 during cell entry is  
885 mediated by VP<sub>5</sub>. *J Virol* 77:7254-60.
- 886 43. Guerrero CA, Bouyssouade D, Zárate S, Isa P, López T, Espinosa R, Romero P,  
887 Méndez E, López S, Arias CF. 2002. Heat shock cognate protein 70 is involved in  
888 rotavirus cell entry. *J Virol* 76:4096-102.
- 889 44. Li B, Ding S, Feng N, Mooney N, Ooi YS, Ren L, Diep J, Kelly MR, Yasukawa LL,  
890 Patton JT, Yamazaki H, Shirao T, Jackson PK, Greenberg HB. 2017. Drebrin restricts  
891 rotavirus entry by inhibiting dynamin-mediated endocytosis. *Proc Natl Acad Sci U S*  
892 *A* 114:E3642-E3651.
- 893 45. Condemine W, Eguether T, Couroussé N, Etchebest C, Gardet A, Trugnan G,  
894 Chwetzoff S. 2019. The C terminus of rotavirus VP<sub>4</sub> protein contains an actin  
895 binding domain which requires cooperation with the coiled-coil domain for actin  
896 remodeling. *J Virol* 93.
- 897 46. Nejmeddine M, Trugnan G, Sapin C, Kohli E, Svensson L, Lopez S, Cohen J. 2000.  
898 Rotavirus spike protein VP<sub>4</sub> is present at the plasma membrane and is associated  
899 with microtubules in infected cells. *J Virol* 74:3313-20.
- 900 47. Trejo-Cerro Ó, Eichwald C, Schraner EM, Silva-Ayala D, López S, Arias CF. 2018.  
901 Actin-dependent nonlytic rotavirus exit and infectious virus morphogenetic  
902 pathway in nonpolarized cells. *J Virol* 92.
- 903 48. Gardet A, Breton M, Fontanges P, Trugnan G, Chwetzoff S. 2006. Rotavirus spike  
904 protein VP<sub>4</sub> binds to and remodels actin bundles of the epithelial brush border into  
905 actin bodies. *J Virol* 80:3947-56.
- 906 49. Gardet A, Breton M, Trugnan G, Chwetzoff S. 2007. Role for actin in the polarized  
907 release of rotavirus. *J Virol* 81:4892-4.
- 908 50. Wolf M, Vo PT, Greenberg HB. 2011. Rhesus rotavirus entry into a polarized  
909 epithelium is endocytosis dependent and involves sequential VP<sub>4</sub> conformational  
910 changes. *J Virol* 85:2492-503.

- 911 51. Predonzani A, Arnoldi F, López-Requena A, Burrone OR. 2008. In vivo site-specific  
912 biotinylation of proteins within the secretory pathway using a single vector system.  
913 BMC Biotechnol 8:41.
- 914 52. De Lorenzo G, Eichwald C, Schraner EM, Nicolin V, Bortul R, Mano M, Burrone OR,  
915 Arnoldi F. 2012. Production of *in vivo*-biotinylated rotavirus particles. J Gen Virol  
916 93:1474-82.
- 917 53. Laimbacher AS, Esteban LE, Castello AA, Abdusetir Cerfoglio JC, Argüelles MH,  
918 Glikmann G, D'Antuono A, Mattion N, Berois M, Arbiza J, Hilbe M, Schraner EM,  
919 Seyffert M, Dresch C, Epstein AL, Ackermann M, Fraefel C. 2012. HSV-1 amplicon  
920 vectors launch the production of heterologous rotavirus-like particles and induce  
921 rotavirus-specific immune responses in mice. Mol Ther 20:1810-20.
- 922 54. Kanai Y, Kobayashi T. 2021. Rotavirus reverse genetics systems: Development and  
923 application. Virus Res 295:198296.
- 924 55. Jiménez-Zaragoza M, Yubero MP, Martín-Forero E, Castón JR, Reguera D, Luque D,  
925 de Pablo PJ, Rodríguez JM. 2018. Biophysical properties of single rotavirus particles  
926 account for the functions of protein shells in a multilayered virus. Elife 7.
- 927 56. Zárate S, Espinosa R, Romero P, Méndez E, Arias CF, López S. 2000. The VP5  
928 domain of VP4 can mediate attachment of rotaviruses to cells. J Virol 74:593-9.
- 929 57. Dormitzer PR, Greenberg HB, Harrison SC. 2000. Purified recombinant rotavirus  
930 VP7 forms soluble, calcium-dependent trimers. Virology 277:420-8.
- 931 58. Shaw RD, Vo PT, Offit PA, Coulson BS, Greenberg HB. 1986. Antigenic mapping of  
932 the surface proteins of rhesus rotavirus. Virology 155:434-51.
- 933 59. Papa G, Venditti L, Arnoldi F, Schraner EM, Potgieter C, Borodavka A, Eichwald C,  
934 Burrone OR. 2019. Recombinant rotaviruses rescued by reverse genetics reveal the  
935 role of NSP5 hyperphosphorylation in the assembly of viral factories. J Virol 94.
- 936 60. Déctor MA, Romero P, López S, Arias CF. 2002. Rotavirus gene silencing by small  
937 interfering RNAs. EMBO Rep 3:1175-80.
- 938 61. Martínez JL, Eichwald C, Schraner EM, López S, Arias CF. 2022. Lipid metabolism is  
939 involved in the association of rotavirus viroplasms with endoplasmic reticulum  
940 membranes. Virology 569:29-36.
- 941 62. Shutova MS, Svitkina TM. 2018. Mammalian nonmuscle myosin II comes in three  
942 flavors. Biochem Biophys Res Commun 506:394-402.
- 943 63. Limouze J, Straight AF, Mitchison T, Sellers JR. 2004. Specificity of blebbistatin, an  
944 inhibitor of myosin II. J Muscle Res Cell Motil 25:337-41.
- 945 64. Trask SD, Dormitzer PR. 2006. Assembly of highly infectious rotavirus particles  
946 recoated with recombinant outer capsid proteins. J Virol 80:11293-304.

- 947 65. Herrmann T, Torres R, Salgado EN, Berciu C, Stoddard D, Nicastro D, Jenni S,  
948 Harrison SC. 2021. Functional refolding of the penetration protein on a non-  
949 enveloped virus. *Nature* 590:666-670.
- 950 66. Abdelhakim AH, Salgado EN, Fu X, Pasham M, Nicastro D, Kirchhausen T, Harrison  
951 SC. 2014. Structural correlates of rotavirus cell entry. *PLoS Pathog* 10:e1004355.
- 952 67. Salgado EN, Garcia Rodriguez B, Narayanaswamy N, Krishnan Y, Harrison SC. 2018.  
953 Visualization of calcium ion loss from rotavirus during cell entry. *J Virol* 92.
- 954 68. Salgado EN, Upadhyayula S, Harrison SC. 2017. Single-particle detection of  
955 transcription following rotavirus entry. *J Virol* 91.
- 956 69. Trask SD, Kim IS, Harrison SC, Dormitzer PR. 2010. A rotavirus spike protein  
957 conformational intermediate binds lipid bilayers. *J Virol* 84:1764-70.
- 958 70. Trejo-Cerro O, Aguilar-Hernández N, Silva-Ayala D, López S, Arias CF. 2019. The  
959 actin cytoskeleton is important for rotavirus internalization and RNA genome  
960 replication. *Virus Research* 263:27-33.
- 961 71. Beckett D, Kovaleva E, Schatz PJ. 1999. A minimal peptide substrate in biotin  
962 holoenzyme synthetase-catalyzed biotinylation. *Protein Sci* 8:921-9.
- 963 72. Fairhead M, Howarth M. 2015. Site-specific biotinylation of purified proteins using  
964 BirA. *Methods Mol Biol* 1266:171-84.
- 965 73. Roux KJ, Kim DI, Burke B. 2013. BioID: a screen for protein-protein interactions. *Curr*  
966 *Protoc Protein Sci* 74:19.23.1-19.23.14.
- 967 74. Vesikari T, Clark HF, Offit PA, Dallas MJ, DiStefano DJ, Goveia MG, Ward RL,  
968 Schödel F, Karvonen A, Drummond JE, DiNubile MJ, Heaton PM. 2006. Effects of  
969 the potency and composition of the multivalent human-bovine (WC<sub>3</sub>) reassortant  
970 rotavirus vaccine on efficacy, safety and immunogenicity in healthy infants. *Vaccine*  
971 24:4821-9.
- 972 75. Ruiz-Palacios GM, Pérez-Schael I, Velázquez FR, Abate H, Breuer T, Clemens SC,  
973 Chevart B, Espinoza F, Gillard P, Innis BL, Cervantes Y, Linhares AC, López P,  
974 Macías-Parra M, Ortega-Barría E, Richardson V, Rivera-Medina DM, Rivera L,  
975 Salinas B, Pavía-Ruz N, Salmerón J, Rüttimeann R, Tinoco JC, Rubio P, Nuñez E,  
976 Guerrero ML, Yarzabal JP, Damaso S, Tornieporth N, Sáez-Llorens X, Vergara RF,  
977 Vesikari T, Bouckennooghe A, Clemens R, De Vos B, O'Ryan M, Group HRVS. 2006.  
978 Safety and efficacy of an attenuated vaccine against severe rotavirus  
979 gastroenteritis. *N Engl J Med* 354:11-22.
- 980 76. Ito N, Takayama-Ito M, Yamada K, Hosokawa J, Sugiyama M, Minamoto N. 2003.  
981 Improved recovery of rabies virus from cloned cDNA using a vaccinia virus-free  
982 reverse genetics system. *Microbiol Immunol* 47:613-7.



- 983 77. Guglielmi KM, McDonald SM, Patton JT. 2010. Mechanism of intraparticle synthesis  
984 of the rotavirus double-stranded RNA genome. *J Biol Chem* 285:18123-8.
- 985 78. Arnold M, Patton JT, McDonald SM. 2009. Culturing, storage, and quantification of  
986 rotaviruses. *Curr Protoc Microbiol* Chapter 15:Unit 15C.3.
- 987 79. Fuerst TR, Niles EG, Studier FW, Moss B. 1986. Eukaryotic transient-expression  
988 system based on recombinant vaccinia virus that synthesizes bacteriophage T7 RNA  
989 polymerase. *Proc Natl Acad Sci U S A* 83:8122-6.
- 990 80. Yusa K, Zhou L, Li MA, Bradley A, Craig NL. 2011. A hyperactive piggyBac  
991 transposase for mammalian applications. *Proc Natl Acad Sci U S A* 108:1531-6.
- 992 81. Papa G, Venditti L, Braga L, Schneider E, Giacca M, Petris G, Burrone OR. 2020.  
993 CRISPR-Csy4-mediated editing of rotavirus double-stranded RNA genome. *Cell Rep*  
994 32:108205.
- 995 82. Kanai Y, Komoto S, Kawagishi T, Nouda R, Nagasawa N, Onishi M, Matsuura Y,  
996 Taniguchi K, Kobayashi T. 2017. Entirely plasmid-based reverse genetics system for  
997 rotaviruses. *Proc Natl Acad Sci U S A* 114:2349-2354.
- 998 83. Komoto S, Kanai Y, Fukuda S, Kugita M, Kawagishi T, Ito N, Sugiyama M, Matsuura  
999 Y, Kobayashi T, Taniguchi K. 2017. Reverse genetics system demonstrates that  
1000 rotavirus nonstructural protein NSP6 is not essential for viral replication in cell  
1001 culture. *J Virol* 91.
- 1002 84. Eichwald C, Vascotto F, Fabbretti E, Burrone OR. 2002. Rotavirus NSP5: mapping  
1003 phosphorylation sites and kinase activation and viroplasm localization domains. *J*  
1004 *Virol* 76:3461-70.
- 1005 85. Sun M, Giambiagi S, Burrone O. 1997. [VP4 protein of simian rotavirus strain SA11  
1006 expressed by a baculovirus recombinant]. *Zhongguo Yi Xue Ke Xue Yuan Xue Bao*  
1007 19:48-53.
- 1008 86. Petris G, Bestagno M, Arnoldi F, Burrone OR. 2014. New tags for recombinant  
1009 protein detection and O-glycosylation reporters. *PLoS One* 9:e96700.
- 1010 87. Bellinzoni RC, Mattion NM, Burrone O, Gonzalez A, La Torre JL, Scodeller EA. 1987.  
1011 Isolation of group A swine rotaviruses displaying atypical electropherotypes. *J Clin*  
1012 *Microbiol* 25:952-4.
- 1013 88. Arnoldi F, Campagna M, Eichwald C, Desselberger U, Burrone OR. 2007. Interaction  
1014 of rotavirus polymerase VP1 with nonstructural protein NSP5 is stronger than that  
1015 with NSP2. *J Virol* 81:2128-37.
- 1016 89. Campagna M, Eichwald C, Vascotto F, Burrone OR. 2005. RNA interference of  
1017 rotavirus segment 11 mRNA reveals the essential role of NSP5 in the virus  
1018 replicative cycle. *J Gen Virol* 86:1481-7.



- 1019 90. Buttafuoco A, Michaelsen K, Tobler K, Ackermann M, Fraefel C, Eichwald C. 2020.  
1020 Conserved rotavirus NSP5 and VP2 domains interact and affect viroplasm. *J Virol*  
1021 94.
- 1022 91. Eichwald C, De Lorenzo G, Schraner EM, Papa G, Bollati M, Swuec P, de Rosa M,  
1023 Milani M, Mastrangelo E, Ackermann M, Burrone OR, Arnoldi F. 2018. Identification  
1024 of a small molecule that compromises the structural integrity of viroplasms and  
1025 rotavirus double-layered particles. *J Virol* 92.
- 1026 92. Glück S, Buttafuoco A, Meier AF, Arnoldi F, Vogt B, Schraner EM, Ackermann M,  
1027 Eichwald C. 2017. Rotavirus replication is correlated with S/G2 interphase arrest of  
1028 the host cell cycle. *PLoS One* 12:e0179607.
- 1029 93. Schindelin J, Arganda-Carreras I, Frise E, Kaynig V, Longair M, Pietzsch T, Preibisch  
1030 S, Rueden C, Saalfeld S, Schmid B, Tinevez JY, White DJ, Hartenstein V, Eliceiri K,  
1031 Tomancak P, Cardona A. 2012. Fiji: an open-source platform for biological-image  
1032 analysis. *Nat Methods* 9:676-82.
- 1033 94. Chen D, Gombold JL, Ramig RF. 1990. Intracellular RNA synthesis directed by  
1034 temperature-sensitive mutants of simian rotavirus SA11. *Virology* 178:143-51.
- 1035 95. Bauer M, Smith GP. 1988. Filamentous phage morphogenetic signal sequence and  
1036 orientation of DNA in the virion and gene-V protein complex. *Virology* 167:166-75.  
1037
- 1038

1039 **Figure Legends**

1040 **Figure 1. Generation of VP<sub>4</sub>-BAP tagged recombinant rotavirus** (a) Schematic  
1041 representation of BAP tag inserted into the lectin domain loops of the VP8\* subunit of VP<sub>4</sub>  
1042 from RV simian strain SA11 (GenBank: X14204.1). The lysine (K, red) indicates the  
1043 biotinylation site of BirA ligase. Four different VP<sub>4</sub> proteins tagged with BAP (VP<sub>4</sub>-BAP)  
1044 were built between amino acid regions T96-R101 (blue), E109-S114 (orange), N132-Q137  
1045 (pink), and K145-G150 (green). VP<sub>4</sub> trimer ribbon structure is presented for the visualization  
1046 of VP8\* (yellow) and VP5CT (body and stalk, red) fragments. An inset in VP8\* indicates the  
1047 different positions in the hydrophobic loops of VP8\* where the BAP tags were inserted and  
1048 colored in blue, orange, pink, and green. (b) Immunoblot retardation assay of cell lysates  
1049 transiently expressing wtVP<sub>4</sub> and VP<sub>4</sub>-BAP, tagged at blue, orange, pink, and green  
1050 positions, respectively. Untreated (-) and streptavidin-treated (+) samples are indicated.  
1051 The membrane was incubated with anti-VP<sub>4</sub> to detect unbound VP<sub>4</sub>-BAP and VP<sub>4</sub>-BAP  
1052 bound to streptavidin (VP<sub>4</sub>-BAP•StAv).  $\alpha$ -tubulin was used as a loading control. (c) dsRNA  
1053 electropherotype of the genome segments of rRV/wt and rRV/VP<sub>4</sub>-BAP. The red arrow  
1054 points to gs<sub>4</sub>-BAP. (d) Sequence chromatogram of gs<sub>4</sub> of rRV/VP<sub>4</sub>-BAP. The sequence  
1055 indicates the position of the linkers and the BAP tag in between the VP8\*. (e)  
1056 Immunoblotting of uninfected (lanes 1 and 4) or infected cell lysates in MA-cytBirA cells  
1057 (left panel) or MA104 cells (right panel) infected with either rRV/wt (lanes 2 and 5) or  
1058 rRV/VP<sub>4</sub>-BAP (lanes 3 and 6) [MOI, 25 VFU/cell]. Biotinylated proteins were detected with  
1059 StAv-HRP.  $\alpha$ -tubulin was used as a loading control. The red arrow and red star indicate  
1060 biotinylated VP<sub>4</sub>-BAP and host undetermined biotinylated protein, respectively. (f)  
1061 Immunoblot retardation assay of MA-cytBirA cell lysates infected with rRV/wt or rRV/VP<sub>4</sub>-  
1062 BAP untreated or treated with StAv. The membrane was incubated with anti-VP<sub>4</sub> and anti-

1063 VP6 for detection of the virus. GAPDH was used as a loading control. The percentage of  
1064 biotinylated VP<sub>4</sub> and VP<sub>4</sub>-BAP was normalized to VP6 expression. **(g)** Visualization at a  
1065 high resolution of purified virions isolated of rRV/VP<sub>4</sub>-BAP infected MA-cytBirA cells  
1066 untreated (-biotin, upper panel) or treated (+biotin, lower panel) with 100µM biotin. After  
1067 purification, the virions were labeled with streptavidin conjugated to colloidal gold (12 nm),  
1068 followed by negative staining electron microscopy (right panel). The scale bar is 100 nm. **(h)**  
1069 Detection of purified unbiotinylated (grey bars) and biotinylated (open bars) rRV/VP<sub>4</sub>-BAP  
1070 particles. The particles were coated in an ELISA plate followed by binding to streptavidin-  
1071 HRP or guinea pig anti-rotavirus followed by anti-guinea pig conjugated to HRP. The  
1072 median from three independent experiments is shown (ordinary one-way ANOVA, \*\*\*\*\*)  
1073 p-value<0.0001). **(i)** Scatter dot plot comparing the diameter of purified particles from  
1074 unbiotinylated (-biotin, filled green dots) or biotinylated (+biotin, open green dots) RV/VP<sub>4</sub>-  
1075 BAP and rRV/wt (filled grey dots). The median value is indicated, n>40 particles, ordinary  
1076 one-way ANOVA, (\*) p-value<0.05 and (\*\*) p-value<0.01.

1077 **Figure 2. RV protein localization upon rRV/VP<sub>4</sub>-BAP infection.** **(a)** rRV/wt (top panel) and  
1078 rRV/VP<sub>4</sub>-BAP (bottom panel) infected MA-cytBirA cells were untreated (-biotin) or treated  
1079 with biotin (+biotin). Cells were fixed with paraformaldehyde at 6 hpi and stained for the  
1080 detection of viroplasm (anti-NSP<sub>5</sub>, green) and biotinylated proteins (streptavidin-Alexa  
1081 555, red). Nuclei were stained with DAPI (blue). **(b)** Immunostaining images of rRV/VP<sub>4</sub>-  
1082 BAP infected MA-cytBirA cells in the presence of biotin. At 6 hpi, paraformaldehyde-fixed  
1083 cells were stained for the detection of VP<sub>4</sub>-BAP (StAv, red) in viroplasm (anti-NSP<sub>5</sub>,  
1084 green) (upper row) or mature RV particles (anti-VP7 clone 159, green) (bottom row). **(c)**  
1085 Immunofluorescence images of cells infected with rRV/wt (upper row) or rRV/VP<sub>4</sub>-BAP  
1086 (lower row) comparing the localization of VP<sub>4</sub> and VP<sub>4</sub>-BAP (anti-VP<sub>4</sub>, red), respectively.

1087 The viroplasm were detected with anti-NSP5 (green). Nuclei were stained with DAPI. In all  
1088 the figures, the dashed white boxes correspond to the image insets of the right columns.  
1089 The yellow arrows point to the VP<sub>4</sub>-BAP or VP<sub>4</sub> signal. The scale bar is 10 μm.

1090 **Figure 3. Replication fitness of rRV/VP<sub>4</sub>-BAP is delayed.** (a) Virus replication fitness curve  
1091 from 0 to 48 hpi of rRV/wt and rRV/VP<sub>4</sub>-BAP. The curve represents the mean of three  
1092 independent experiments. Welch's t-test, (\*), p<0.05; (\*\*\*), p<0.001 and ns, not significant.  
1093 Quantification of cells with viroplasm of MA<sub>104</sub> cells infected rRV/wt and rRV/VP<sub>4</sub>-BAP at  
1094 (b) same MOI (25 VFU/cell) or (c) the same numbers of virus particles.

1095 **Figure 4. Virus attachment and internalization of RV/wt and rRV/VP<sub>4</sub>-BAP are**  
1096 **comparable.** (a) Virus attachment to MA<sub>104</sub> cell surface with different amounts of purified  
1097 rRV/wt (open grey dots) and rRV/VP<sub>4</sub>-BAP (full green dots). Samples were detected using a  
1098 guinea pig anti-RV. The result corresponds to the mean of nine normalized independent  
1099 experiments. Data analysis corresponds to nonlinear regression, p=0.2987, n=9. Virus  
1100 attachment assay to MA<sub>104</sub> cell surface with different amounts of unbiotinylated (-biotin,  
1101 full green dots) and biotinylated (+biotin, green open dots) purified rRV/VP<sub>4</sub>-BAP detected  
1102 with (b) guinea pig anti-RV followed by secondary antibody conjugated to HRP. Data  
1103 analysis corresponds to nonlinear regression, p=0.6151, n=6. (c) Same as above, but  
1104 samples were detected with streptavidin-HRP. Data analysis corresponds to nonlinear  
1105 regression, p<0.0001, n=6. (d) Internalization of purified virions into MA<sub>104</sub> cells at 0 min  
1106 (upper panel) and 2 min (lower panel). Purified virions of rRV/wt and biotinylated rRV/VP<sub>4</sub>-  
1107 BAP were previously labeled with StAv-Alexa 555 (red). At the indicated time post-  
1108 infection, cells were fixed and immunostained for VP7 trimers (mAb anti-VP7 clone 159,  
1109 pink) and MTs (anti- α-tubulin, green). Nuclei were stained with DAPI (blue). White open  
1110 boxes indicate the magnified images at the right. Arrows point to virus particle clumps

1111 detected by anti-VP7. The scale bar is 20  $\mu\text{m}$ . **(e-g)** Plots from quantitative RT-PCR  
1112 comparing rotavirus transcripts of NSP5, VP6, and housekeeping gene (SDHA) in non-  
1113 infected (NI), rRV/wt- and rRV/VP<sub>4</sub>-BAP-infected cellular extracts at 4 hpi. The results  
1114 correspond to the mean  $\pm$  SEM of three independent experiments, ordinary one-way  
1115 ANOVA, (\*\*),  $p < 0.01$ ; (\*\*\*),  $p < 0.001$ ; (\*\*\*\*),  $p < 0.0001$ .

1116 **Figure 5. Viroplasm morphology and behavior for rRV/wt and rRV/VP<sub>4</sub>-BAP. (a)**  
1117 Representative high-resolution electron micrograph of viroplasms from rRV/wt (upper row)  
1118 and rRV/VP<sub>4</sub>-BAP (lower row) infected MA<sub>104</sub> cells at 6 hpi (left panel) and 12 hpi (right  
1119 panel). Scale bars are 200nm and 500 nm, as indicated. **(b)** Fluorescence images of FRAP  
1120 measurement of single viroplasm of cells infected with rRV/VP<sub>4</sub>-BAP (top) and rRV/wt  
1121 (bottom) at pre-bleach, post-bleach, and recovery time conditions. Each inset indicates the  
1122 bleached viroplasm of the images at the right. Nuclei were stained with Hoechst 33342. The  
1123 scale bar is 10  $\mu\text{m}$ . **(c)** FRAP recovery curve of NSP2-mCherry in single viroplasm from  
1124 rRV/VP<sub>4</sub>-BAP (green) and rRV/wt (grey) infected MA/NSP2-mCherry cells at 5 hpi (n=27 and  
1125 25, respectively). Plots indicating recovery half-time **(d)** and diffusion **(e)** means of NSP2-  
1126 mCherry in single viroplasms of rRV/VP<sub>4</sub>-BAP and rRV/wt after photobleaching.

1127 **Figure 6. Transfection of rRV/VP<sub>4</sub>-BAP DLPs is inefficient in forming viroplasms. (a)** Size  
1128 plot of TLPs and DLPs purified from rRV/wt and rRV/VP<sub>4</sub>-BAP. The median value is  
1129 indicated, n>30 particles, ordinary one-way ANOVA, (\*) p-value<0.05 and (\*\*\*\*) p-  
1130 value<0.0001. **(b)** In-cell western blot of MA<sub>104</sub> cells transfected for 4 h with identical  
1131 numbers of rRV/wt and rRV/VP<sub>4</sub>-BAP DLPs. RV infection was detected by staining with  
1132 anti-NSP5 (IDye800, red). The loading control corresponds to cell tag 700 (green). The  
1133 merge of the two channels is shown at the bottom. **(c)** Plot showing normalized amounts of  
1134 NSP5 in rRV/wt and rRV/VP<sub>4</sub>-BAP-DLPs transfected MA<sub>104</sub> cells. Each experiment was

1135 done in triplicate. **(d)** Micrograph of rRV/wt and rRV/VP<sub>4</sub>-BAP DLPs transfected MA<sub>104</sub>  
1136 cells immunostained to detect viroplasms with anti-NSP<sub>5</sub> (green). Nuclei were stained with  
1137 DAPI (blue). Open dashed white box shows enlarged viroplasm inset at the right. The scale  
1138 bar is 10 μm. **(e)** Quantification of the cells showing viroplasms upon transfection with DLPs  
1139 of rRV/wt and rRV/VP<sub>4</sub>-BAP. The data correspond to the mean ± SD, Welch's t-test, (\*\*\*\*),  
1140  $p > 0.0001$ .

1141 **Figure 7. VP<sub>4</sub> has a role in viroplasm formation.** **(a)** Schematic representation for the  
1142 characterization of LLPS condensates in viroplasms of RV-infected cells. At 5 hpi, RV-  
1143 infected MA/NSP<sub>2</sub>-mCherry cells were treated with 1,6-HD for 6 min. The drug was washed  
1144 out, and samples were fixed and imaged for viroplasm quantification at 0-, 2-, 15- and 30-  
1145 min post-recovery. **(b)** Representative images of MA/NSP<sub>2</sub>-mCherry cells infected at 5 hpi  
1146 with rRV/wt (upper row) or rRV/VP<sub>4</sub>-BAP (lower row) and treated with 3.5% of 1,6-HD. Cells  
1147 were washed and monitored for viroplasm formation at 0-, 2-, 15- and 30-min post-  
1148 recovery. White arrows point to cells with recovered viroplasms. The scale bar is 10 μm.  
1149 Plots indicating the ratio of cells with viroplasms **(c)** and viroplasm counts per cell **(d)**  
1150 normalized at initial conditions (5 hpi). **(e)** Immunoblot of cellular extracts prepared at 6 hpi  
1151 from non-infected or SA<sub>11</sub>-infected MA<sub>104</sub> or MA/NSP<sub>2</sub>-mCherry cells silenced with siVP<sub>4</sub>  
1152 or control siRNA (scr). The membrane was stained with anti-VP<sub>4</sub>, anti-NSP<sub>5</sub>, and anti-  
1153 GAPDH (loading control). **(f)** Representative images of SA<sub>11</sub>-infected MA/NSP<sub>2</sub>-mCherry  
1154 cells knocked down with scr (upper row) or siVP<sub>4</sub> (lower row) and treated for 6 min with  
1155 3.5% of 1,6-HD. Cells were washed and monitored for viroplasm formation at 0-, 2-, 15- and  
1156 30-min post-recovery. White arrows point to cells showing recovered viroplasms. The scale  
1157 bar is 10 μm. Plot indicating the ratio of cells with viroplasms **(g)** and viroplasm counts per  
1158 cell **(h)** normalized to initial conditions after recovery from 1,6-HD treatment of SA<sub>11</sub>-

1159 infected MA104 cells silenced with siVP<sub>4</sub> or scr The data represent the mean ± SEM  
1160 Student's t-test (\*), p<0.05; and (\*\*\*), p<0.001.

1161 **Figure 8. VP<sub>4</sub>-BAP does not bind to the actin cytoskeleton. (a)** Immunostaining of  
1162 MA104 cells showing NSP<sub>5</sub> and NSP<sub>2</sub> VLSs co-expressed with GFP (top panel), VP<sub>4</sub>-GFP  
1163 (middle panel), and VP<sub>4</sub>-BAP-GFP (bottom panel). Cells were fixed with paraformaldehyde  
1164 and immunostained to detect VLSs (anti-NSP<sub>5</sub>, red). Nuclei were stained with DAPI (blue).  
1165 The scale bar is 10 μm. **(b)** Plot indicating the number of VLSs per cell when co-expressed  
1166 with GFP, VP<sub>4</sub>-GFP, and VP<sub>4</sub>-BAP-GFP. The data represent the mean ± SEM, one-way  
1167 ANOVA, (\*), p<0.05 and (\*\*), p<0.001. **(c)** Immunostaining of MA104 cells expressing VP<sub>4</sub>-  
1168 GFP and VP<sub>4</sub>-BAP-GFP after treatment for 1 h before fixation without (-NOC) or with  
1169 (+NOC) 10 μM nocodazole. Cells were fixed with methanol at 24 hpt and immunostained  
1170 for GFP detection (anti-GFP, green) and actin cytoskeleton (anti-actin, red). Nuclei were  
1171 stained with DAPI (blue). The scale bar is 10 μm. **(d)** Plot for the quantification of VP<sub>4</sub>-GFP  
1172 and VP<sub>4</sub>-BAP-GFP filament lengths associated with actin filaments in cells untreated or  
1173 treated with nocodazole. The data represent the mean ± SD, Welch's t-test, (\*\*\*\*),  
1174 p<0.0001.

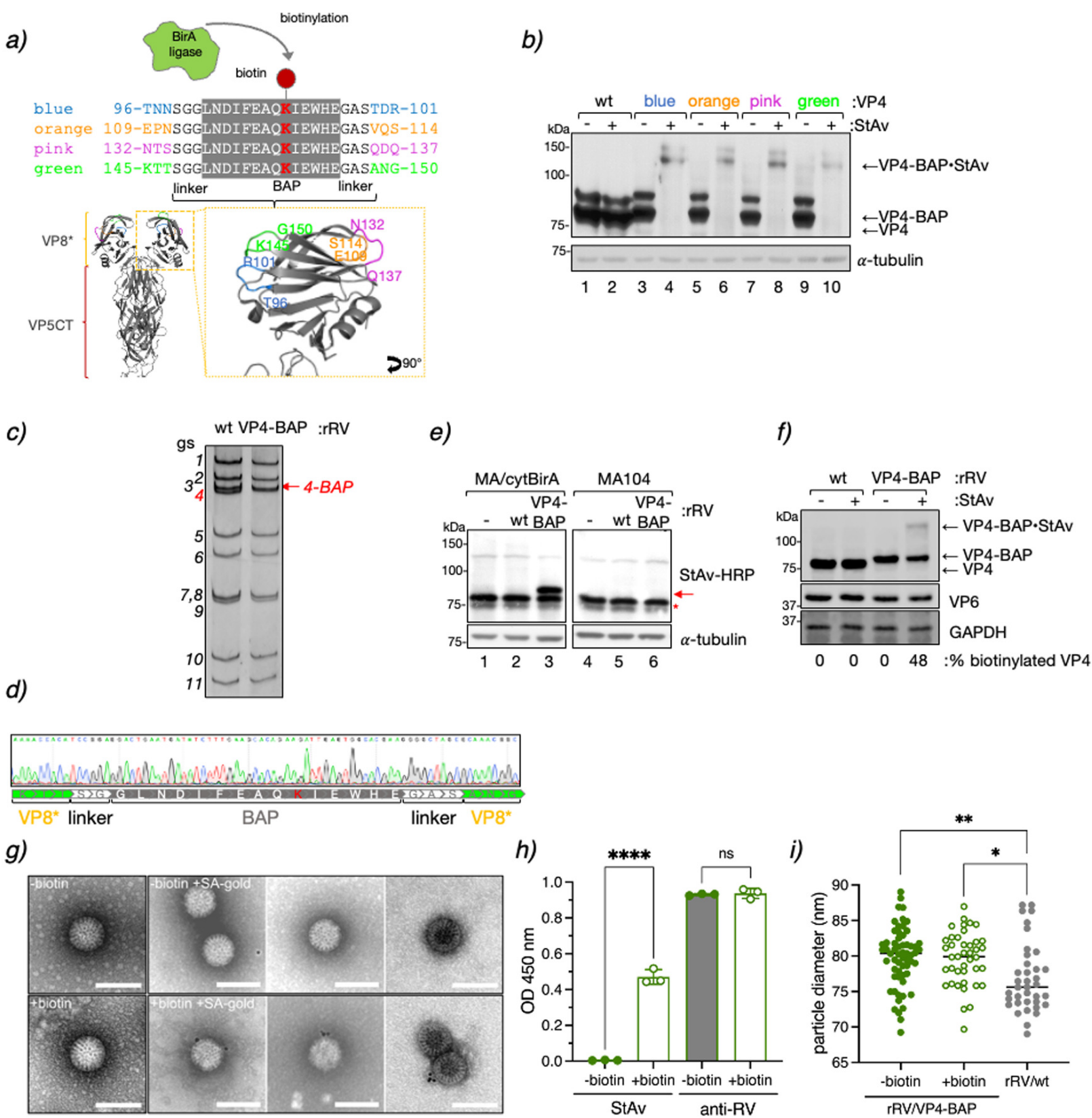
1175 **Figure 9. rRV/VP<sub>4</sub>-BAP impaired association with the actin cytoskeleton. (a)**  
1176 Immunostaining of non-infected and SA11-infected MA104 cells. At 6 hpi, cells were fixed  
1177 with methanol and immunostained to detect viroplasms (anti-NSP<sub>5</sub>, green) and actin  
1178 cytoskeleton (anti-actin, cyan). Nuclei were stained with DAPI (blue). The scale bar is 20  
1179 μm. Immunostaining of non-infected and rRV/wt or rRV/VP<sub>4</sub>-BAP-infected MA104 cells. At  
1180 6 hpi, cells were fixed with methanol and immunostained for detection of **(b)** VP<sub>4</sub> (anti-  
1181 VP<sub>4</sub>, green) and actin cytoskeleton (anti-actin, cyan) and **(c)** VP<sub>4</sub> (anti-VP<sub>5</sub> clone 4G<sub>2</sub>, cyan)  
1182 and myosin motor (anti-myosin IIa, green). Nuclei were stained with DAPI (blue). The scale

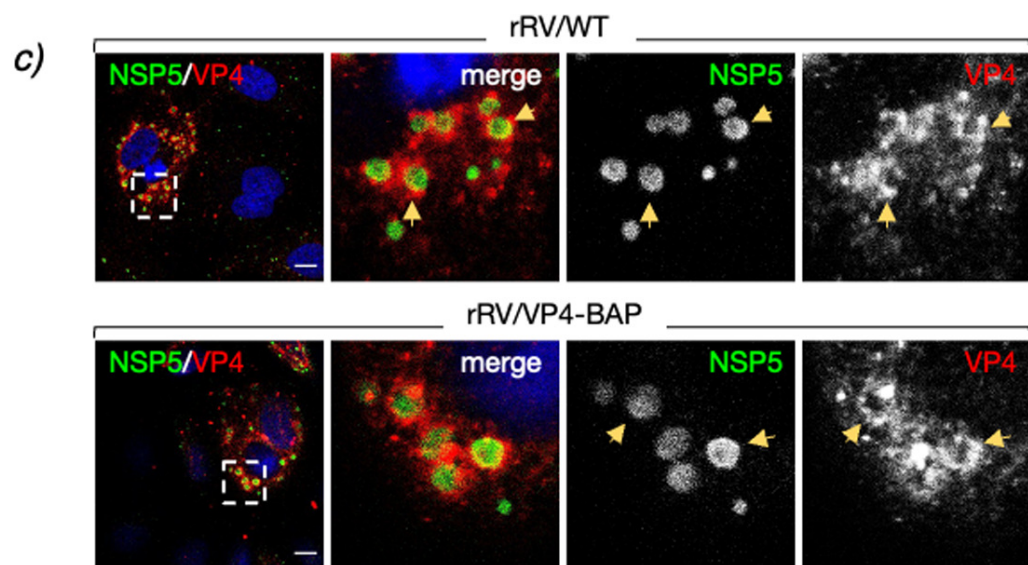
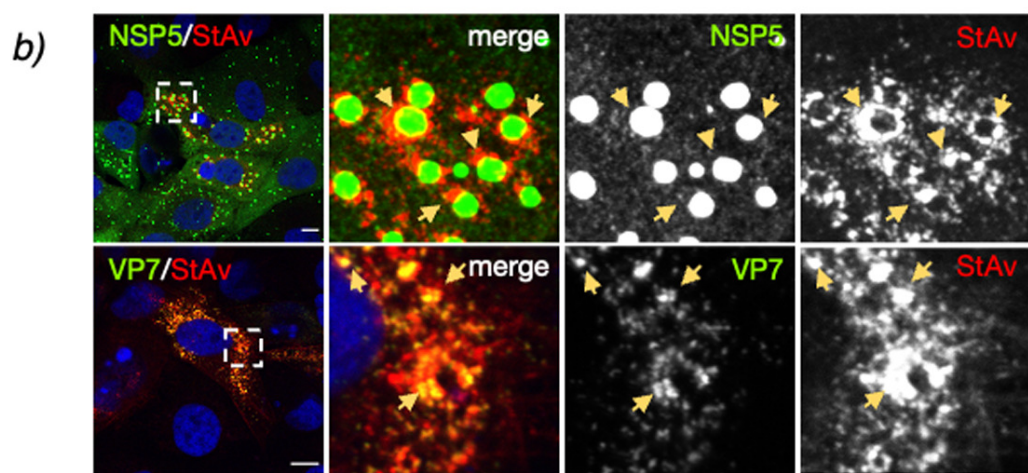
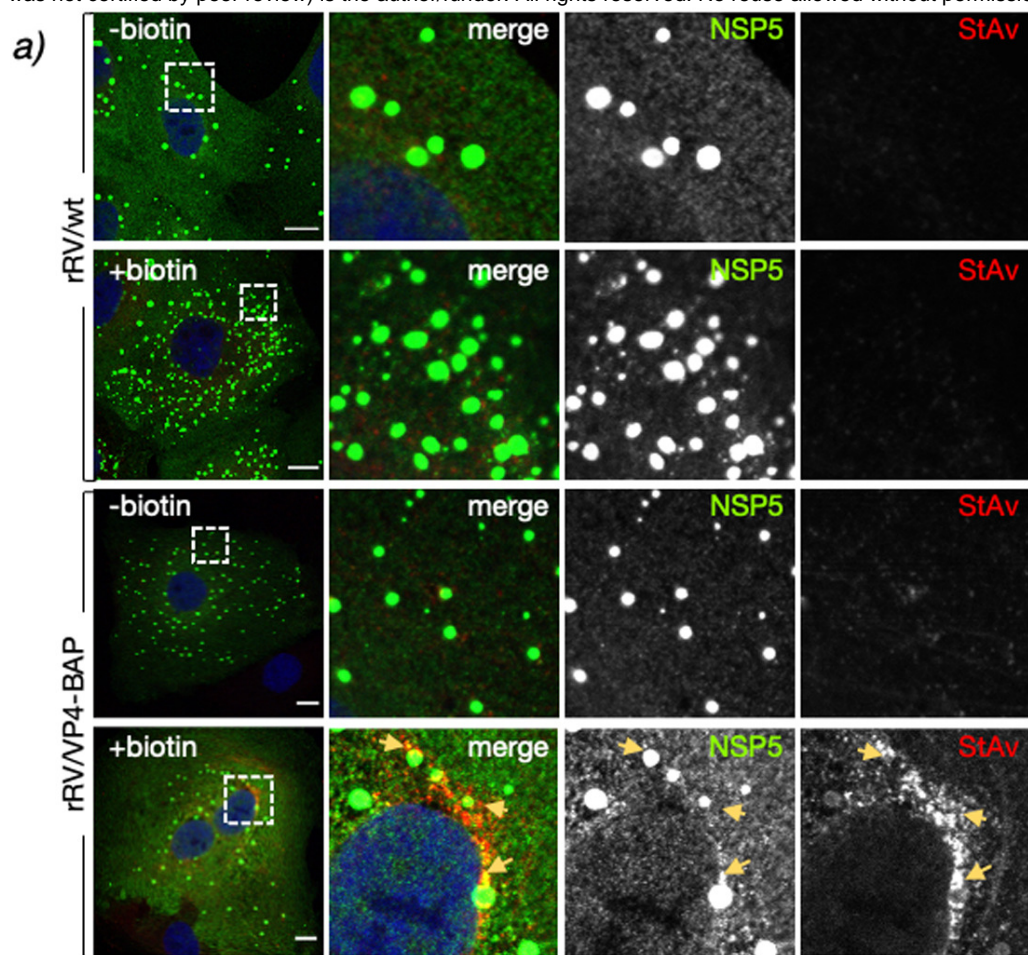
1183 bar is 20  $\mu\text{m}$ . Open yellow and red arrowheads point to stress fibers in the actin  
1184 cytoskeleton and VP<sub>4</sub> fibers, respectively. **(d)** Immunofluorescence of rRV/wt and rRV/VP<sub>4</sub>-  
1185 BAP-infected MA10<sub>4</sub> cells treated at 1 hpi with either 0.5  $\mu\text{M}$  jasplakinolide (jasp; middle  
1186 panel) or 10  $\mu\text{M}$  cytochalasin B (cyt B; lower panel). At 6 hpi, cells were fixed and  
1187 immunostained to detect viroplasms (anti-NSP<sub>5</sub>, green). Nuclei were stained with DAPI  
1188 (blue). The dashed open box corresponds to the inset of the enlarged image at the right.  
1189 The scale bar is 10  $\mu\text{m}$ . Plot for the quantification of **(e)** the ratio of cells showing viroplasms  
1190 and **(f)** the number of viroplasms per cell. **(g)** Immunofluorescence of rRV/wt and rRV/VP<sub>4</sub>-  
1191 BAP- infected MA10<sub>4</sub> cells untreated or treated at 1 hpi with 5  $\mu\text{M}$  blebbistatin (BLB). At 6  
1192 hpi, cells were fixed and immunostained to detect viroplasms (anti-NSP<sub>5</sub>, green). Nuclei  
1193 were stained with DAPI (blue). The dashed open box is an inset of the enlarged image at  
1194 the right. The scale bar is 10  $\mu\text{m}$ . Plot for the quantification of **(h)** the ratio of cells showing  
1195 viroplasms and **(i)** the number of viroplasms per cell.

1196 **Figure 10. A peptide mimicking loop K145-G150 rescues the rRV/VP<sub>4</sub>-BAP phenotype.**  
1197 **(a)** Immunofluorescence images at 17 hpt of BHK-T<sub>7</sub> cells expressing VP<sub>4</sub>-GFP or VP<sub>4</sub>-BAP-  
1198 GFP, untreated or treated with 25  $\mu\text{M}$  SPL added immediately after transfection. Before  
1199 methanol fixation, cells were treated for 1 h with 10  $\mu\text{M}$  nocodazole. The cells were  
1200 immunostained for GFP (anti-GFP, red), and nuclei were stained with DAPI (blue). Scale bar  
1201 is 10  $\mu\text{m}$ . **(b)** Plot quantifying the length of VP<sub>4</sub> filaments untreated or treated with SPL as  
1202 described in **(a)**. Welch ANOVA test, (\*\*),  $p < 0.01$  and (\*\*\*\*),  $p < 0.0001$ . **(c)** Representative  
1203 immunofluorescence microphotograph of viroplasms of rRV/wt and rRV/VP<sub>4</sub>-BAP -infected  
1204 cells untreated (-SPL) or treated (+SPL) at +1 and +3 hpi with 25  $\mu\text{M}$  of SPL, as indicated.  
1205 Viroplasms were immunostained at 6 hpi with anti-NSP<sub>5</sub> (red), and nuclei were stained with  
1206 DAPI (blue). The dashed white boxes correspond to the enlarged picture in the right

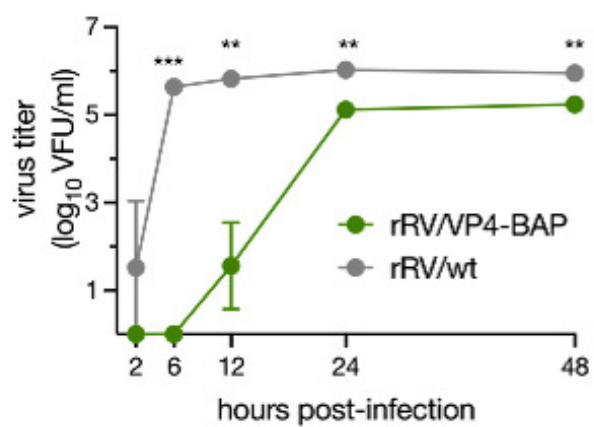


1207 columns. Scale bar is 10  $\mu$ m. Quantification plots for the ratio of cells with viroplasms **(d)**  
1208 and the numbers **(e)** and size **(f)** of viroplasms per cell of MA104 cells infected with the  
1209 indicated virus and untreated (UT) or treated with 25  $\mu$ M SPL at +1 and +3 hpi. The data  
1210 represent the mean  $\pm$  SEM using Welch's ANOVA test, (\*\*\*)  $p < 0.001$  and (\*\*\*\*),  
1211  $p < 0.0001$ . **(g)** Plot determining the virus progeny of rRV/wt and rRV/BAP infected cells  
1212 untreated or treated at 1 hpi with 25  $\mu$ M SPL. The data represent the mean  $\pm$  SEM of three  
1213 independent experiments. Welch ANOVA test, (\*)  $p < 0.05$ .  
1214

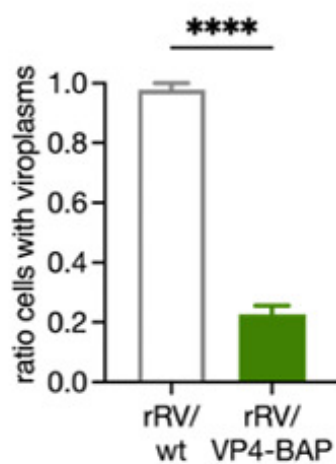




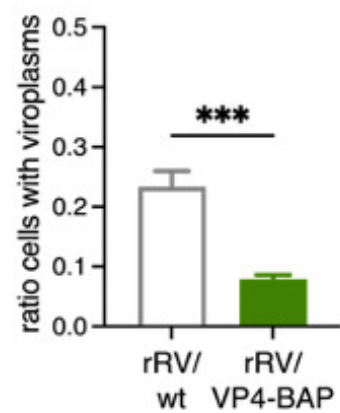
a)



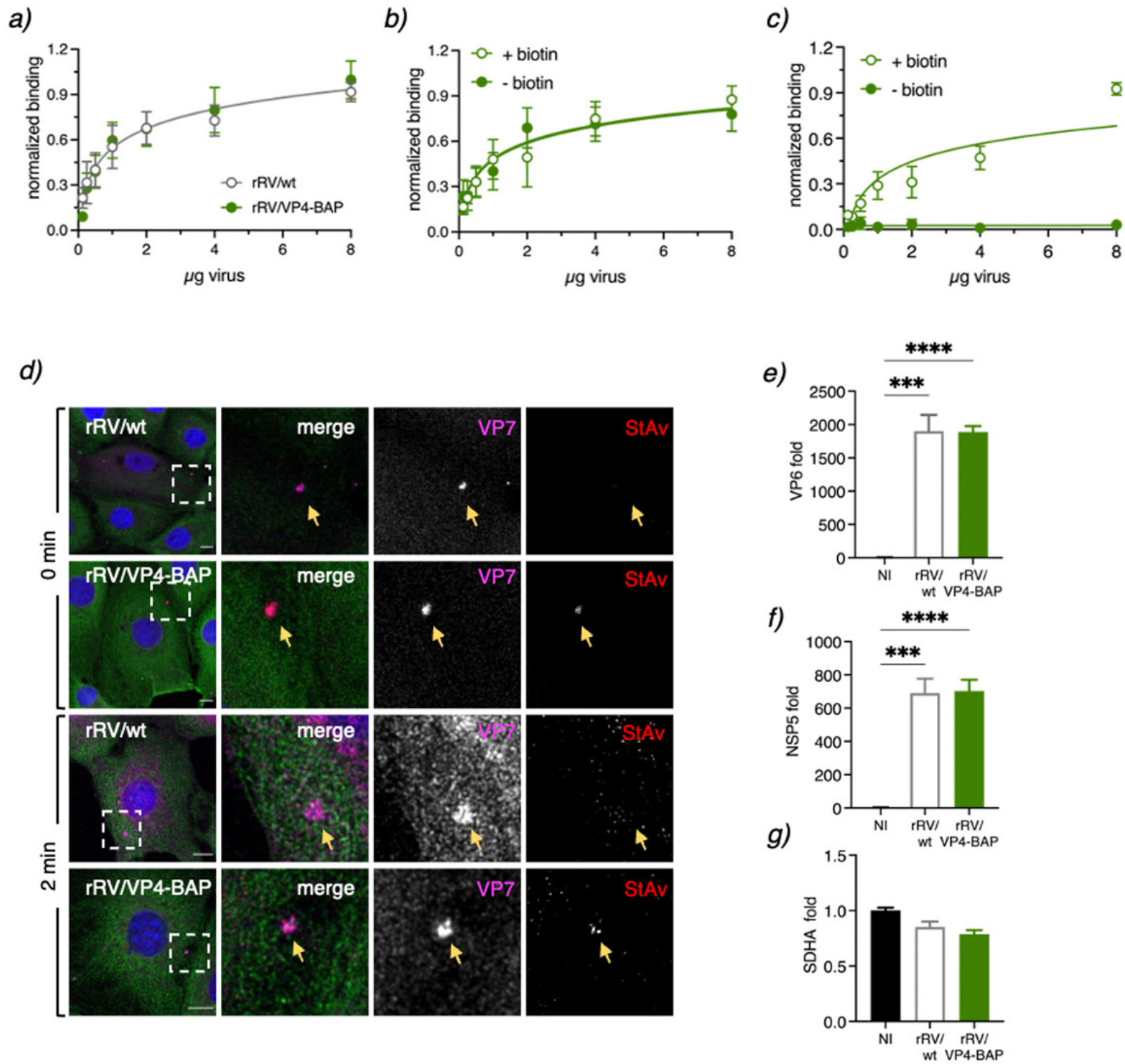
b)



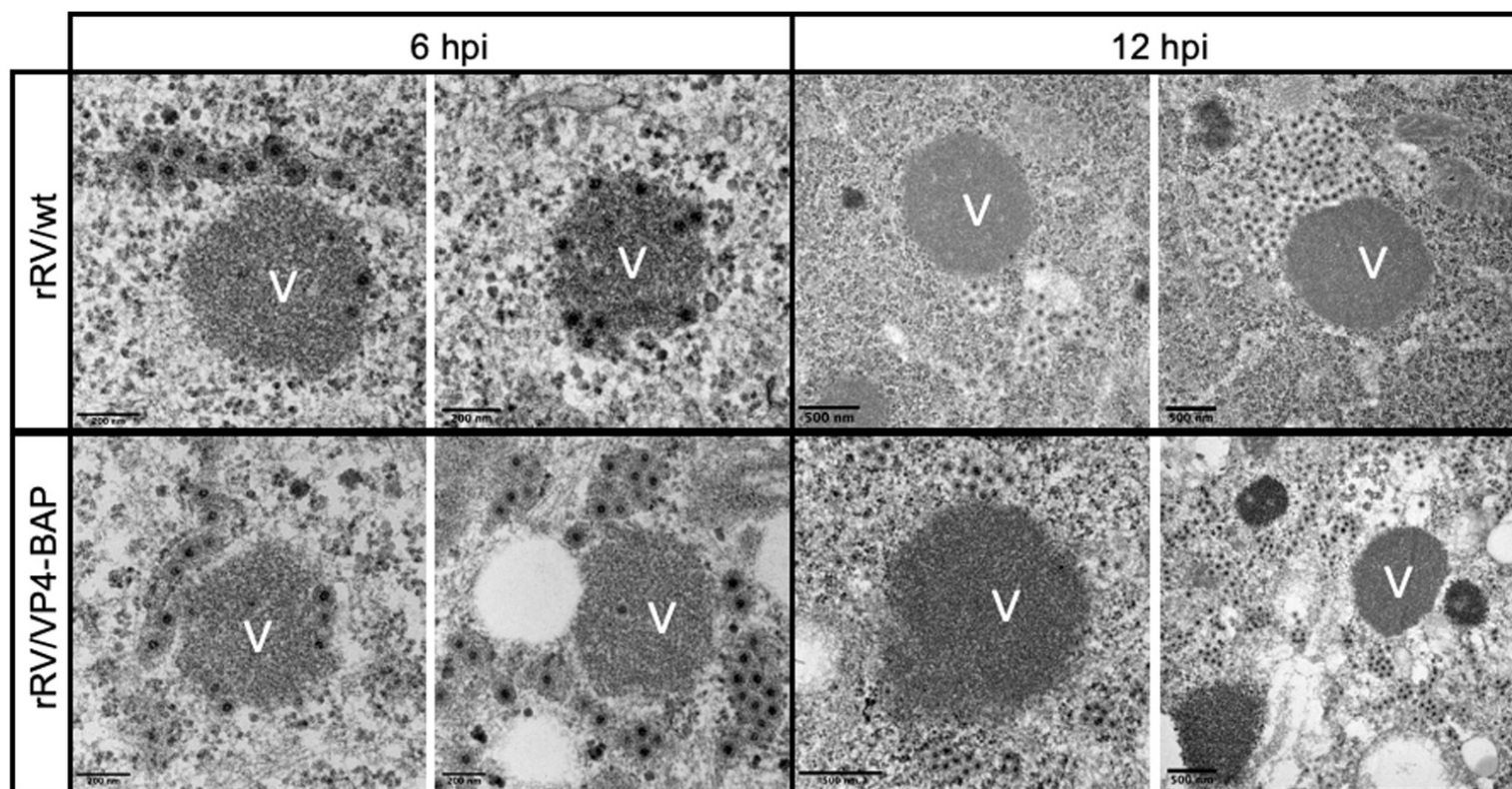
c)



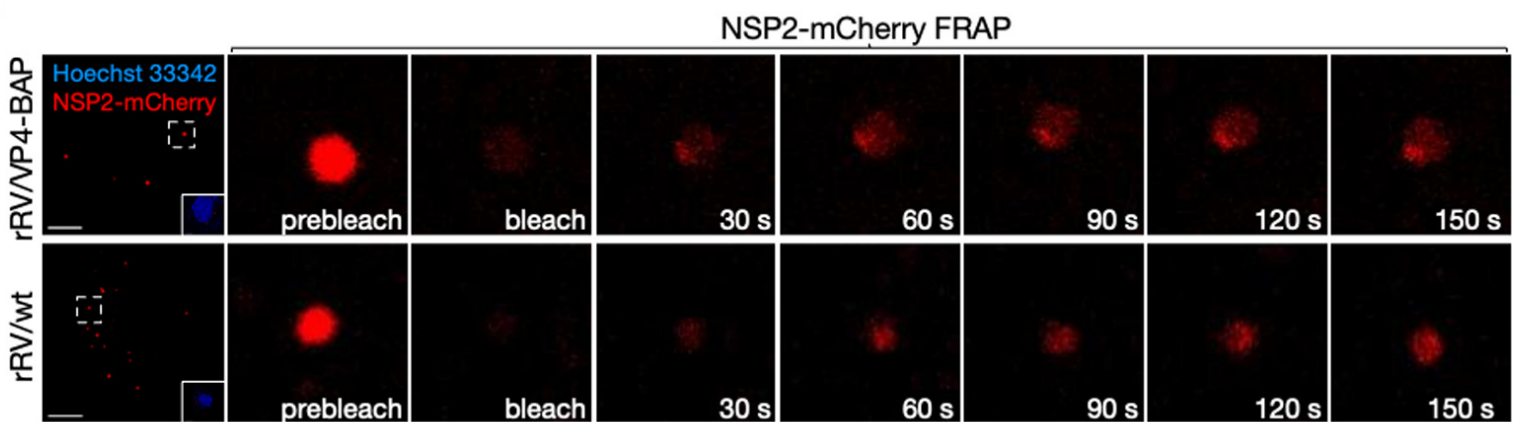




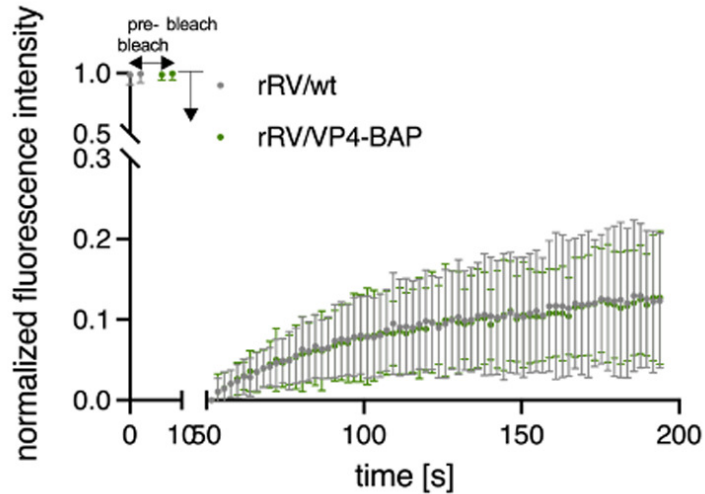
a)



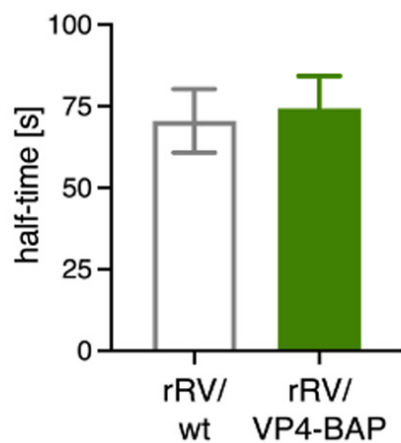
b)



c)



d)



e)

